HHS Public Access

Author manuscript

Cell. Author manuscript; available in PMC 2024 August 21.

Published in final edited form as:

Cell. 2021 September 16; 184(19): 4981–4995.e14. doi:10.1016/j.cell.2021.08.004.

The Immunostimulatory RNA RN7SL1 Enables CAR-T Cells to Enhance Autonomous and Endogenous Immune Function

Lexus R. Johnson[1,2,3,4,6], **Daniel Y. Lee**[1,3], **Jacqueline S. Eacret**[1,3], **Darwin Ye**[1,3], **Carl H. June**[2,3,4,5,6,*], **Andy J. Minn**[1,3,5,6,*]

[1]Department of Radiation Oncology, Immune Signaling, and Radiation, Perelman School of Medicine, University of Pennsylvania, Philadelphia, PA, USA

[2]Department of Pathology and Laboratory Medicine, Immune Signaling, and Radiation, Perelman School of Medicine, University of Pennsylvania, Philadelphia, PA, USA

[3]Abramson Family Cancer Research Institute, Immune Signaling, and Radiation, Perelman School of Medicine, University of Pennsylvania, Philadelphia, PA, USA

[4]Center for Cellular Immunotherapies, Immune Signaling, and Radiation, Perelman School of Medicine, University of Pennsylvania, Philadelphia, PA, USA

[5]Parker Institute for Cancer Immunotherapy, Immune Signaling, and Radiation, Perelman School of Medicine, University of Pennsylvania, Philadelphia, PA, USA

[6]Mark Foundation Center for Immunotherapy, Immune Signaling, and Radiation, Perelman School of Medicine, University of Pennsylvania, Philadelphia, PA, USA

SUMMARY

Poor tumor infiltration, development of exhaustion, and antigen insufficiency are common mechanisms that limit CAR-T cell efficacy. Delivery of pattern recognition receptor agonists is one strategy to improve immune function; however, targeting these agonists to immune cells is challenging, and off-target signaling in cancer cells can be detrimental. Here, we engineer CAR-T cells to deliver RN7SL1, an endogenous RNA that activates RIG-I/MDA5 signaling. RN7SL1 promotes expansion and effector-memory differentiation of CAR-T cells. Moreover, RN7SL1 is

*Co-corresponding authors: Andy J. Minn (andyminn@upenn.edu), Carl H. June (cjune@upenn.edu).

AUTHOR CONTRIBUTIONS

L.R.J. designed and conducted experiments, analyzed and interpreted the data, and prepared the manuscript. D.Y.L., J.S.E., and D.Y. assisted with in vitro and in vivo assays. C.H.J. and A.J.M. led the design, interpretation, and analysis of all experiments, and the preparation of the manuscript.

Lead Contact Andy J. Minn, MD, PhD, 421 Curie Blvd, BRB II/III, Room 510, Philadelphia, PA 19104

DECLARATION OF INTERESTS

A.J.M. has received research funding from Merck. He is a scientific advisor for Takeda, H3Biomedicine, and Xilio. A.J.M. is an inventor on patents related to the IFN pathway, and A.J.M., L.R.J., and C.H.J. are inventors on a filed patent related to modified CAR T cells. C.H.J. reports research funding from Novartis, and he is a scientific founder of Tmunity Therapeutics. A.J.M., C.H.J., and L.R.J. are scientific founders for Project 5 Therapeutics. C.H.J. also works under a research collaboration involving the University of Pennsylvania and the Novartis Institute of Biomedical Research, Inc. and is an inventor of intellectual property licensed by the University of Pennsylvania to Novartis.

deployed in extracellular vesicles and selectively transferred to immune cells. Unlike other RNA agonists, transferred RN7SL1 restricts MDSC development, decreases TGFB in myeloid cells, and fosters DC subsets with costimulatory features. Consequently, endogenous effector-memory and tumor-specific T cells also expand, allowing rejection of solid tumors with CAR antigen loss. Supported by improved endogenous immunity, CAR-T cells can now co-deploy peptide antigens with RN7SL1 to enhance efficacy even when heterogenous CAR antigen tumors lack adequate neoantigens.

In-brief

CAR-T cells expressing an immunostimulatory RNA achieve enhanced efficacy in solid tumor mouse models with CAR antigen loss by improving autonomous CAR-T cell function and promoting endogenous immunity through preferential uptake of RNA-containing extracellular vesicles in innate immune cells over tumor cells.

Graphical Abstract

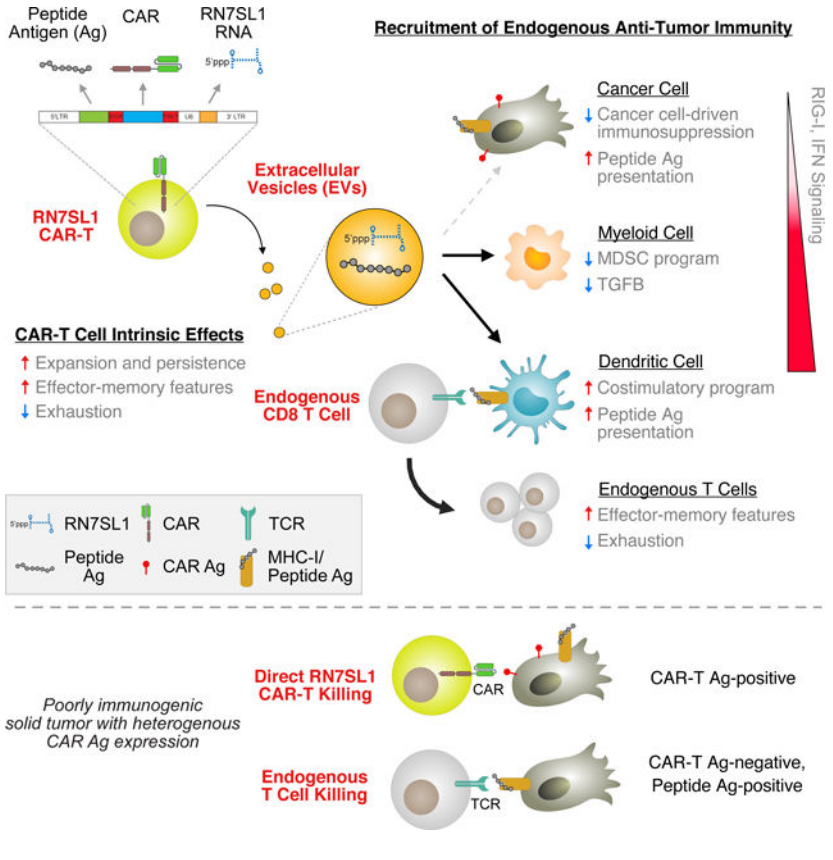

INTRODUCTION

Chimeric antigen receptor (CAR) T cells have generated remarkable outcomes in the treatment of a small subset of hematopoietic cancers but remain ineffective in the majority of solid tumors. Factors that contribute to poor efficacy in solid tumors include limited expansion and persistence of transferred cells in the tumor microenvironment (TME),

which has motivated efforts to improve intrinsic functionality of CAR-T cells (Majzner and Mackall, 2019). However, even when CAR-T cells do successfully engage tumor targets, resistance can result from outgrowth of cancer cells that have lost expression of CAR antigens (Gardner et al., 2016; Sotillo et al., 2015). In contrast to adoptive cell therapy, immune checkpoint blockade (ICB) typically stimulates endogenous T cells of multiple specificities to yield a polyclonal anti-tumor response (Keskin et al., 2019; Wu et al., 2020). For both CAR-T cell and ICB therapy, expression of negative immunoregulatory proteins like PDL1 (Liu et al., 2016) and production of suppressive cytokines like TGFB (Kloss et al., 2018; Roth et al., 2020; Tang et al., 2020) within the TME are additional barriers that impede immunotherapy response. Thus, strategies that simultaneously employ CAR-T cells, enhance endogenous T cell function, and counteract common suppressive mechanisms may offer effective combinatorial approaches to improve solid tumor response.

Damage-associated molecular patterns (DAMPs) act as ligands for pattern recognition receptors (PRRs) that signal tissue injury and/or pathogen invasion. The activation of PRRs can initiate an innate immune response that is a prerequisite for mounting successful adaptive immunity. RIG-I and MDA5 are cytoplasmic PRRs that typically recognize virus-encoded double stranded RNA (dsRNA), often with a 5’-triphosphate (Hur, 2019). Upon activation, these PRRs aggregate with the MAVS signaling platform to enhance production of interferon (IFN) and induce transcription of IFN-stimulated genes (ISGs). Such innate immune signaling is particularly important for myeloid and dendritic cells (DCs) to effectively prime and/or activate T cells (Kandasamy et al., 2016). Recent evidence demonstrates that endogenous nucleic acids can also serve as DAMPs to activate PRRs. RN7SL1 (7SL) is a highly structured noncoding RNA that is present in all cell types and conserved from humans to bacteria (Denks et al., 2014). Under homeostatic conditions, RN7SL1 functions as a scaffold crucial for protein translation (Halic and Beckmann, 2005). In this role, several RNA binding proteins shield it from recognition by cytosolic RNA PRRs. However, under pathological conditions, decreased interaction with RNA binding proteins enables RN7SL1 to become unshielded and secreted via extracellular vesicles (EVs) such as exosomes (Nabet et al., 2017). Consequently, unshielded RN7SL1 mimics viral RNA to activate a RIG-I-dependent inflammatory response in cancer cells and myeloid cells.

Although DAMPs can activate PRRs, their effectiveness in augmenting anti-tumor immunity depends on multiple factors. First, the consequences of inducing a type I IFN (IFN-I) or type II IFN response in immune cells versus cancer cells can be complex and even opposing. While PRR and IFN signaling in immune cells such as dendritic cells (DCs) can be immunostimulatory, signaling in cancer cells can drive cancer progression (Nabet et al., 2017) and immunotherapy resistance (Benci et al., 2019; Benci et al., 2016). The immunosuppressive effects of cancer cell-intrinsic activation of ISGs are thought to occur through multiple mechanisms that include induction of immune inhibitory genes and genes that influence immune-mediated tumor killing. Second, due to low mutation burden and immunoediting in most human cancers, the lack of strong neoantigens can make the endogenous T cell repertoire ill-equipped for effective tumor eradication (Schumacher and Schreiber, 2015). This paucity of strong neoantigens severely limits the utility of employing PRR activation to augment endogenous T cell priming. Thus, both directing

PRR signaling toward immune cells rather than cancer cells and developing approaches to deliver neoantigens to tumors are needed to maximize the efficacy of cancer immunotherapy.

In this study, we show how multiple limitations of CAR-T cells against solid tumors can be addressed by decoding complexities of IFN/PRR signaling and then engineering CAR-T cells to deploy RN7SL1 to recode these signals in the TME. RN7SL1 CAR-T cells exhibit enhanced intrinsic function, selectively activate RIG-I in immune cells, and can be further equipped to co-deliver peptide antigens. The result is a multi-armored CAR-T cell that effectively infiltrates tumors, productively activates myeloid and dendritic cells, provisions the TME with antigens, and primes endogenous T cells to reject solid tumors under threat of CAR antigen loss.

RESULTS

Biasing PRR activation away from cancer cells improves immunotherapy response

We produced *in vitro* transcribed RN7SL1 and a control RNA with the same nucleotide composition as RN7SL1 but scrambled in its sequence (Scr). With both RNAs, a ribozyme sequence was used to generate a uniform 3’ end. RN7SL1 has extensive RNA secondary structure, while the Scr RNA is predicted to lack widespread dsRNA regions (Nabet et al., 2017). Both RNAs have a 5’-triphosphate, which is a feature that promotes recognition by RIG-I. Compared to cellular RNA, which is primarily comprised of ribosomal RNA with a 5’-monophosphate, transfection of RN7SL1 into B16-F10 melanoma cells or human DCs induces ISGs such as MHC-I, PDL1, and CD86 (Fig. 1A and S1A–B). ISG induction also occurs after transfection with poly I:C, which serves as a positive control, or with the Scr RNA. Interestingly, the ability of RN7SL1 to stimulate ISGs is dependent on both RIG-I and MDA5. In contrast, Scr RNA and poly I:C only require one PRR or the other. Thus, although RN7SL1 and Scr RNA both induce ISGs, RN7SL1 utilizes both RIG-I and MDA5, indicating distinct signaling mechanisms.

To determine the consequence of RN7SL1 and Scr RNA recognition *in vivo* we implanted B16 tumors into the flanks of wildtype mice and injected liposome-encapsulated RNA intratumorally. While cellular and Scr RNA have minimal effects compared to a liposome-only control, intratumoral injection of RN7SL1 enhances tumor growth and decreases survival in T cell-deficient mice following antibody-mediated depletion of CD4 and CD8 T cells (Fig. 1B). These results are consistent with our previous findings demonstrating that the activation of RIG-I by RN7SL1 in cancer cells can promote tumor growth and metastasis in an immunocompromised setting (Nabet et al., 2017). To determine the effect of RN7SL1 when the immune system is intact and activated, mice were instead treated with immune checkpoint blockade consisting of anti-PD1 plus anti-CTLA4. In this context, intratumoral injection of RN7SL1 improves ICB response, while Scr and cellular RNA continue to have minimal effect (Fig. 1C and S1C). Accordingly, RN7SL1 augments infiltration of activated and proliferating CD8 and/or CD4 T cells (Fig. 1D and S1D), as well as enhances the frequency of intratumoral DCs (Fig. 1E and S1E). Thus, these results suggest that although stimulation of cancer cell-intrinsic RIG-I can promote tumor growth, this deleterious effect can be offset by the ability of RN7SL1 to also promote anti-tumor immunity.

Considering that activating cancer cell-intrinsic RIG-I can enhance tumor growth, we reasoned that it also might negatively impact immune function even in the presence of ICB. Indeed, when B16 melanoma cells with RIG-I knockout are implanted into flanks of mice and then treated with intratumoral RN7SL1 plus anti-CTLA4 and anti-PD1, tumor response is improved compared to control wildtype B16 tumors (Fig. 1F). In contrast, the absence of RIG-I in cancer cells does not affect response to ICB alone, indicating that the negative impact of cancer cell RIG-I signaling occurs in the presence of stimulatory RNA. In total, these findings suggest that although RN7SL1 can enhance immunotherapy, its activation of RIG-I in cancer cells can contribute to suboptimal response (Fig. 1G). Thus, strategies that bias delivery of RN7SL1 away from cancer cells in favor of immune cells might improve the efficacy of immunotherapy.

RN7SL1 expressed by CAR-T cells improves autonomous CAR-T cell function and tumor control

We hypothesized that one strategy to preferentially activate RN7SL1 in immune cells rather than cancer cells is to utilize a CAR-T cell that expresses RN7SL1 and infiltrates a tumor after having activated an intrinsic IFN response. To examine this approach, we utilized both human and mouse CAR-T cell models. For human CAR-T cells, we chose two CARs currently in clinical trials: the M5BBz CAR against human mesothelin or the 19BBz CAR (tisagenlecleucel) against human CD19. For later experiments utilizing mouse CAR-T cells, primary murine T cells were transduced with a retrovirus to express the CAR. Downstream of the M5BBz and 19BBz CAR sequence is a U6 promoter that drives transcription of either human RN7SL1 or the Scr control RNA (Fig. 2A). For mouse CAR-T cells, both RN7SL1 and Scr RNA are constitutively detected (Fig. S2A) and surface levels of the co-expressed CAR are comparable (Fig. S2B). In human CAR-T cells, RN7SL1 and the M5BBz CAR are also readily detected (Fig. S2C–D) but expression of the Scr RNA appears toxic (data not shown), prompting us to rely on the M5BBz CAR construct as the control.

We first investigated whether RN7SL1 has cell autonomous effects on CAR-T cells. To do this, we examined phenotypic markers for activation/differentiation in human healthy donor T cells transduced with a CAR co-expressing RN7SL1 or CAR alone. After CAR-T cell expansion, expression of RN7SL1 results in a greater proportion of effector-memory CAR-T cells in all donors examined, as determined by CD45RO and CCR7, suggesting a cell autonomous effect of RN7SL1 pre-infusion (Fig. 2B and S2E). Next, we used M5BBz CAR-T cells expressing RN7SL1 (M5BBz-7SL) or M5BBz alone to treat NSG mice xenografted with human ASPC-1 pancreatic tumors that endogenously express mesothelin (MSLN). This revealed that RN7SL1 significantly improves the antitumor efficacy of M5BBz CAR-T cells and results in durable responses (Fig. 2C) that are not associated with weight loss or other significant toxicity (Fig. S2F). Single-cell RNA sequencing (scRNA-seq) of human cells from ASPC-1 tumors seven days after treatment demonstrated a large proportion of MSLN-positive cancer cells but also identified infiltrated CAR-T cells, as assessed by *TRAC* and other human T cell-related genes (Fig. 2D). As expected, M5BBz-7SL CAR-T cells exhibit higher expression of type I IFN-stimulated genes (ISGs) compared to M5BBz CAR-T cells (Fig. 2D–E). Moreover, this increase in ISG enrichment from expressing RN7SL1 most strongly impacts CAR-T cells compared to cancer and other cell types in

the tumor. The majority of these infiltrated M5BBz-7SL CAR-T cells continue to exhibit a predominantly memory T cell phenotype (CAR-Tmem), as assessed by enrichment for genes associated with effector/central memory CD8 T cells and, to a lesser extent, terminal effector cells (Fig. 2F–H). In contrast, most M5BBz CAR-T cells are transcriptionally distinct and appear exhausted (CAR-Tex) even at this early timepoint, as characterized by high levels of exhaustion-related gene sets and marker genes like *PD1*, *TIGIT*, *TOX*, and *CD38*, and low levels of genes such as *TCF7* (Fig. 2F, right). Flow cytometry at day 14–17 revealed M5BBz-7SL CAR-T cells also show greater expansion and/or persistence in both tumor (Fig. 2I) and blood (Fig. 2J) with a greater proportion in the periphery having an effector-memory phenotype (Fig. 2K). At day 31, RN7SL1 continues to promote accumulation of M5BBz CAR-T cells with a less exhausted phenotype (Fig. 2L), suggesting that the pre-infusion effects of RN7SL1 are retained throughout the life of the adoptively transferred cells. Together, these results suggest that expressing RN7SL1 in CAR-T cells can preferentially activate IFN/PRR signaling in the CAR-T cell compartment. This results in a cell autonomous effect in human CAR-T cells that initiates productive differentiation, expansion, and durable solid tumor control.

CAR-T cells preferentially deliver RN7SL1 to endogenous immune cells via extracellular vesicles

Our previous work demonstrated that RN7SL1 can be transferred between different cell types in the TME through exosomes (Nabet et al., 2017). Therefore, we reasoned that in addition to a cell autonomous effect, expression of RN7SL1 by CAR-T cells might also result in its export by extracellular vesicles (EVs) that could preferentially activate IFN signaling in endogenous immune cells rather than cancer cells. Indeed, the Scr RNA and RN7SL1 (assayed using primers specific to human RN7SL1) are detected in purified EVs secreted by either mouse or human CAR-T cells (Fig. 3A and S3A). To fully assess the immune consequences of RN7SL1 in EVs, we utilized our mouse 19BBz CAR-T cell system in immunocompetent syngeneic mice. The fluorescent RNA-specific dye Syto RNASelect (SytoRNA) was used to label the RNA of congenically-marked CD45.1$^+$ mouse CAR-T cells (MacDiarmid et al., 2009) prior to transfer into CD45.2$^+$ mice bearing mouse B16-F10 melanoma tumors expressing human CD19 (B16-h19) (Fig. 3B). We found a significant fraction of endogenous CD45.2$^+$ immune cells, including myeloid cells, DCs, and other T cells, are labeled with the SytoRNA dye indicative of RNA transfer from CAR-T cells (Fig. 3C, top). This transfer is diminished after inhibiting EV secretion with GW4869 (Catalano and O'Driscoll, 2020), a neutral sphingomyelinase inhibitor (Fig. 3C, bottom). Examination of sorted SytoRNA$^+$ CD45.2$^+$ intratumoral immune cells by qRT-PCR revealed that RN7SL1 or Scr RNA from 19BBz CAR-T cells is among the RNA transferred to endogenous immune cells (Fig. 3D). Flow cytometry on CD45.2$^+$ immune cells and cancer cells revealed that this transfer of EV RNA from CAR-T cells to immune cells is significantly greater than to cancer cells (Fig. 3E), a selectivity that is not observed with liposome-mediated delivery (Fig. S3B). Thus, these results indicate that RN7SL1 expressed by CAR-T cells is transferred to various cells in the TME through EVs and selectively accumulates in endogenous intratumoral immune cells compared to cancer cells.

CAR-T cell delivery of RN7SL1 is coupled to CAR engagement and improves solid tumor response in immunocompetent mice

While RN7SL1 has a cell autonomous effect that improves CAR-T cell efficacy in NSG mice bearing pancreatic tumor xenografts, its transfer to endogenous immune cells in an immune-competent setting might unleash additional benefits by engaging the host immune system. We surmised that unveiling this effect of RN7SL1 would require ICB to antagonize immunosuppressive mechanisms limiting endogenous immunity typical of poorly immunogenic syngeneic tumors. Indeed, when syngeneic mice harboring B16-h19 tumors are treated with mouse 19BBz CAR-T cells expressing RN7SL1 (19BBz-7SL), only a modest improvement is observed over 19BBz CAR-T cells expressing Scr RNA (19BBz-Scr) or 19BBz alone (Fig. 3F). This suggests that the cell autonomous benefit of RN7SL1 on CAR-T cell function is inadequate in this setting. However, when anti-CTLA4 is added, delivery of RN7SL1 by CAR-T cells markedly enhances tumor response compared to untransduced (UTD) or 19BBz-Scr CAR-T cells (Fig. 3G and S3C–D), an effect not observed with systemic delivery of liposomal RN7SL1 (Fig. S3E). Treatment with 19BBz-7SL CAR-T cells is accompanied by greater infiltration of both CAR-T and endogenous immune cells into the TME (Fig. 3H). The ability of RN7SL1 to improve CAR-T efficacy is also observed in other syngeneic mouse models and with anti-PD1. This includes a typically immunotherapy refractory $Kras^{LSL\text{-}G12D/+};p53^{flox/flox}$ lung cancer model expressing human CD19 (KP-h19) that also exhibits preferential RNA transfer from CAR-T cells to immune cells (Fig. S3G–H), and a TC1 lung cancer model engineered to express human mesothelin and targeted using the M5BBz CAR combined with anti-PD1 instead of anti-CTLA4 (Fig. S3I). Importantly, RN7SL1 expression or delivery by adoptively transferred T cells against endogenously expressed tumor self-antigens also improves tumor response without obvious on-target off-tumor side-effects when combined with ICB (Fig. S3J–K). Together, these data suggest that RN7SL1 can safely improve CAR-T cell efficacy when the endogenous immune system is recruited using ICB.

To investigate requirements for the transfer of RN7SL1 from CAR-T cells to endogenous immune cells, we next labeled resting human 19BBz-7SL CAR-T cells with SytoRNA dye and stimulated with cognate CD19 beads to activate the CAR (Blanchard et al., 2002). This revealed a significant increase in RNA transfer from CAR-T cells to donor-matched PBMCs that is similar to the transfer after stimulation with CD3/CD28 beads used as a positive control (Fig. 3I). The role of CAR engagement in 19BBz-7SL efficacy was also examined *in vivo* by treating CD19-negative B16 tumors with murine 19BBz-7SL CAR-T cells (Fig. 3J) or B16-h19 tumors with M5BBz-7SL CAR-T cells (Fig. S3L). Both cases revealed that CAR target interactions are required for the improved tumor response mediated by RN7SL1. In total, these results suggest that selective delivery of RN7SL1 to immune cells is promoted following CAR-target interactions. In an immune-competent host, this transfer is associated with improved CAR-T cell efficacy.

Delivery of RN7SL1 by CAR-T cells improves immunostimulatory properties of myeloid and DC subsets

To understand how delivery of RN7SL1 from CAR-T cells to endogenous immune cells enhances their function, we repeated scRNA-seq studies using syngeneic B16-h19 tumors

implanted into CD45.2$^+$ mice and treated with 19BBz-7SL, 19BBz-Scr, or 19BBz CAR-T cells congenically marked with CD45.1$^+$ and without ICB (Fig. S4A–C). Consistent with *in vitro* transfection studies showing that both RN7SL1 and Scr RNA stimulate ISGs (Fig. 1A), CAR-T cell delivery of either RN7SL1 or Scr RNA induces ISGs across various CD45.2$^+$ immune cells (Fig. S4D). Since myeloid and DC populations, which also express *Rig-I* and *Mda5* (Fig. S4E), show the strongest induction of ISGs, we more closely interrogated these innate immune populations. For this, we inferred differentiation trajectory and cell states, and then used gene sets for myeloid subsets to assign each state (Fig. 4A–B). Myeloid cells with immunosuppressive properties were evaluated using gene sets for myeloid derived suppressor cells (MDSCs) and by expression of *Tgfb1*. Although both RN7SL1 and Scr RNA increases ISGs across multiple myeloid states (Fig. 4C), only delivery of the Scr RNA leads to a greater accumulation of myeloid cells belonging to the Mdsc.1 and Mdsc.2 states that exhibit the greatest enrichment in MDSC genes (Fig. 4D and S4F–G), including individual markers such as *Cd84* and *Arg2* (Fig. S4H). Conversely, delivery of RN7SL1 decreases levels of *Tgfb1*, which is highly expressed in myeloid states that are largely distinct from the MDSC-like states (Fig. 4E). Thus, although RN7SL1 and Scr RNA both stimulate an IFN response, only delivery of RN7SL1 by CAR-T cells limits MDSC accumulation and expression of *Tgfb1* across multiple myeloid cell types.

To define changes in DCs, myeloid cells along the monocytic DC trajectory were separately clustered and then assigned using gene sets for DC subsets. Four major DC subsets including DC1 (characterized by *Xcr1*, *Clec9a*), DC2 (characterized by *Itgam*, *Sirpa*), DC3 (characterized by *Ccr7*), and plasmacytoid DC (pDC) (characterized by *Siglech*, *Cd7*, and *Cd209a*) were identified along with a fifth cluster primarily comprised of monocytic DCs (Fig. 4F–G and S4I–J). Potential stimulatory properties of each subset were also evaluated using several DC gene regulatory modules (Maier et al., 2020) that include a co-stimulatory module (*Cd80*, *Cd86*, *Cd40*, *Relb*, *Cd83*) and an inhibitory immunoregulatory module (*Cd274*, *Pdcd1lg2*, *Cd200*). As with the myeloid states, both RN7SL1 and Scr RNA increases ISG expression to varying degrees in some but not all DC subsets (Fig. 4H). However, delivery of RN7SL1 but not Scr RNA results in two main effects. First, RN7SL1 increases the frequency of a pDC-like cluster, which was confirmed by flow cytometry for CD209a (Fig. 4I–J). Second, RN7SL1 promotes favorable changes in key regulatory gene modules expressed by the DC1 subset – specifically, there is an enrichment for the co-stimulatory module but a decrease in the inhibitory immunoregulatory module (Fig. 4K). This favorable change in the ratio of costimulatory to inhibitory genes was confirmed using flow cytometry that showed an increase in DCs expressing CD86 rather than PDL1 (Fig. 4L and S4K).

In total, these findings suggest that improvements in the tumor immune infiltrate mediated by RN7SL1 transfer from CAR-T cells is not simply from activation of an IFN response. RN7SL1 restricts the development of suppressive myeloid states and promotes the development of inflammatory DCs with a potent anti-viral and costimulatory phenotype.

Delivery of RN7SL1 by CAR-T cells improves the function of endogenous CD8 T cells

In addition to favorable effects on DCs and myeloid cells in the tumor, RN7SL1 delivered by CAR-T cells also enhances immune infiltration and alters the proportion of different CD8 T cell subsets (Fig. 3H and S4B). To more deeply understand the changes in intratumoral CD8 T cells, we extended our scRNA-seq analysis of B16-h19 tumors to non-naïve CD8 T cells (Fig. 5A and S5A). Here, each CD8 T cell state was first defined as exhausted or non-exhausted, and then refined using additional gene sets for CD8 T cell subsets. This revealed that RN7SL1 delivered by 19BBz-7SL CAR-T cells promotes an increase in effector-like T cells (Teff) and effector-memory-like T cells (Tem) that express *Klrg1* and/or *Tcf7* (Fig. 5B–D). Conversely, there is a decrease in *Tox*-expressing exhausted T cells (Tex), particularly exhausted T cells belonging to a progenitor subset (Tex.prog) that typically progress to terminal exhaustion (Tex.term) after ICB (Beltra et al., 2020). In comparison, delivery of Scr RNA results in effects that appear intermediate between 19BBz and 19BBz-7SL CAR-T cells. These changes in CD8 T cell subsets were corroborated by flow cytometry using ITGB7 as a marker for Teff and Tem, and TOX as a marker for Tex (Fig. 5C and 5E–F; Fig. S5B). Thus, delivery of RN7SL1 by CAR-T cells fosters development and persistence of endogenous CD8 T cells with effector-memory-like properties rather than features of T cell exhaustion.

We surmised that favorable changes in myeloid/DC subsets in the TME after RN7SL1 delivery by CAR-T cells may contribute to the improvements seen in endogenous CD8 T cells. To test this, we utilized mouse BMDCs stimulated with or without RN7SL1 and assayed their capacity to activate OT-I CD8 T cells against the ovalbumin (Ova) peptide antigen SIINFEKL (Fig. 5G, left). Here, stimulation of BMDCs with liposome-encapsulated RN7SL1 is sufficient to enhance OT-I T cell proliferation and production of effector proteins such as GZMB and IFNG (Fig. 5G, right; Fig. S5C). A similar effect is observed using EV RNA isolated from 19BBz-7SL CAR T cells (Fig. 5H). Consistent with RN7SL1 activating RIG-I and/or MDA5, the stimulatory effects of RN7SL1 are largely abrogated with BMDCs from MAVS or RIG-I knockout mice (Fig. 5G and S5D). Indeed, RN7SL1 stimulation of BMDCs also enhances production of type one IFNs (Fig. 5I) and blocking the IFN-I receptor with an anti-IFNAR antibody interferes with OT-I T cell activation (Fig. 5J). In contrast, direct stimulation of activated splenic T cells with RN7SL1 or Poly I:C did not result in enhanced effector function (Fig. S5E). Thus, these results suggest that RN7SL1 deployed by CAR-T cells can directly elicit favorable changes in myeloid/DC subsets that help activate endogenous CD8 T cells.

Armored CAR-T cells that deliver RN7SL1 orchestrate endogenous immune activation

The ability of RN7SL1 to restrict development of suppressive myeloid cells, promote productive CD8 T cell differentiation, and stimulate DCs through RIG-I to prime CD8 T cells *in vitro* all suggest that CAR-T cells armed with RN7SL1 can orchestrate a productive endogenous immune response to enhance CAR-T efficacy. To investigate this notion, we first determined how endogenous T cells and DCs influence response with 19BBz-7SL CAR-T cells plus ICB. Indeed, when *Tcra* knockout mice that lack endogenous T cells are implanted with B16-h19 tumors, survival after 19BBz-7SL CAR-T cell treatment is only modestly different from the UTD control, while 19BBz CAR-T cells show no significant

difference (Fig. 6A). Similar results are observed with *Batf3* knockout mice (Fig. 6B), which specifically lack the DC1 population (Fig. S6A–B) that preferentially expresses costimulatory versus inhibitory genes after 19BBz-7SL CAR-T cell treatment (Fig. 4K). In the absence of DC1s, there is a decrease in the tumor infiltration of endogenous CD8 T cells but only a modest decrement in CAR-T cells (Fig. 6C). Similarly, when wildtype mice are treated with FTY720, which prevents T cell egress from lymphoid tissue, CAR-T cell infiltration is again only modestly impacted (Fig. 6D), while endogenous immune infiltrates largely comprised of activated $Ki67^+$ host T cells are markedly reduced (Fig. 6E). Together, these results suggest that the ability of RN7SL1 to improve CAR-T cell efficacy depends on endogenous CD8 T cells that are primed by DCs in lymphoid tissue and then recruited to the tumor.

To confirm that the ability of RN7SL1 to activate IFN-I signaling through RIG-I/MAVS in DCs is critical for improved CAR-T cell efficacy *in vivo*, we utilized RIG-I knockout mice. *Rig-I*$^{-/-}$ mice exhibit embryonic lethality and rare offspring are born at sub-Mendelian ratios; nonetheless, we procured a small cohort and treated mice bearing B16-h19 tumors with 19BBz-7SL CAR-T cells plus ICB. In contrast to the effects from knocking out RIG-I in cancer cells (Fig. 1F), RIG-I knockout mice (Fig. 6F) and WT mice reconstituted with *Rig-I*$^{-/-}$ bone marrow (Fig. 6G) both exhibit decreased survival, suggesting that RIG-I signaling in host hematopoietic cells is required for the therapeutic benefit of 19BBz-7SL treatment. Accordingly, treatment of mice with anti-IFNAR antibody similarly interferes with 19BBz-7SL CAR-T cell efficacy (Fig. 6H). This is accompanied by a marked failure of RN7SL1 to enhance the frequency of the DC1 subset (Fig. 6I), to increase the proportion of $ITGB7^+$ Teff and Tem cells (Fig. 6J), or to augment the abundance of CD8 and/or CD4 T cells expressing GZMB or Ki67 (Fig. 6K and S6C–D). In total, these results corroborate that intratumoral delivery of RN7SL1 by CAR-T cells orchestrates a productive endogenous anti-tumor immune response by activating RIG-I and IFN signaling in bone marrow-derived cells.

Multi-armored CAR-T cells deploying RN7SL1 and peptide antigens overcome resistance from CAR antigen loss

The requirement for endogenous CD8 T cells for 19BBz-7SL CAR-T cell efficacy in the immunocompetent setting suggests that this CAR-T cell strategy is capable of targeting non-CAR antigens for solid tumor clearance. TRP2 is an immunodominant B16-F10 melanoma self-antigen that can mediate tumor rejection (Bloom et al., 1997). Examination using a TRP2 tetramer (Fig. S7A) reveals that TRP2-specific CD8 T cells express higher levels of GZMB and Ki67 in mice treated with 19BBz-7SL CAR-T cells compared to 19BBz or 19BBz-Scr CAR-T cells (Fig. 7A). This increase is also blocked by anti-IFNAR (Fig. 7A and S7B). Given these effects on tumor-reactive endogenous T cells, we reasoned that 19BBz-7SL CAR-T cells might be less susceptible to resistance arising from loss of CAR antigen. To simulate this common resistance mechanism, we implanted mice with a 1:1 mix of $CD19^+$ and $CD19^-$ B16 tumor cells. While anti-CTLA4 plus 19BBz or 19BBz-Scr CAR-T cells are largely ineffective, use of 19BBz7SL CAR-T cells eradicate these heterogenous tumors comparably to pure B16-h19 tumors (Fig. 7B, Fig. 3G). Mice treated with 19BBz-7SL CAR-T cells that had a complete response were then rechallenged

at day 80 with a WT B16 tumor lacking human CD19. Here, the majority of mice remain tumor-free at 160+ days, consistent with the generation of protective T cell memory against non-CAR tumor antigens (Fig. S7C). Thus, arming CAR-T cells with the ability to deploy RN7SL1 results in the activation of endogenous tumor-reactive effector-memory T cells, making CAR-T cells less susceptible to resistance due to CAR antigen loss.

Many solid human tumors lack sufficient neoantigens and/or an adequate anti-tumor T cell repertoire, either of which might limit endogenous T cell responses initiated by CAR-T cells expressing RN7SL1. To address this, we sought to engineer CAR-T cells to co-deliver RN7SL1 with peptide antigens of choice. As proof of concept, we engineered 19BBz CAR-T cells to express the SIINFEKL peptide alone (Ova-19BBz) or with RN7SL1 (Ova-19–7SL) (Fig. 7C, top). Using an antibody that detects SIINFEKL in complex with MHC-I (Porgador et al., 1997), we confirmed that this peptide is effectively presented on Ova-19BBz CAR-T cells and is also detected on CAR-negative T cells (Fig. 7C, bottom), suggesting successful expression and deployment of this peptide antigen. Indeed, when EVs from Ova-19BBz CAR-T cell cultures are incubated with B16 tumor cells, a dose-dependent increase in SIINFEKL presentation by MHC-I on cancer cells is observed (Fig. 7D, top row, left plot), and addition of naïve OT-I T cells shows increasing T cell activation (Fig. 7D). Parallel *in vivo* experiments reveal that Ova-19BBz CAR-T cells deliver SIINFEKL for presentation on MHC-I by tumor cells and CD45.2^{+} immune cells (Fig. 7E), promote the expansion of Ki67^{+} Ova-specific and total endogenous CD8 T cells (Fig. 7F–G), and improve control of mixed CD19^{+} and CD19^{-} B16 tumors (Fig. 7H). Unlike RNA delivery by CAR-T cells, SIINFEKL delivery was not obviously biased toward immune cells (Fig. S7D). Thus, CAR-T cells can be engineered to deliver peptide antigens that are effectively presented by tumor and immune cells.

Having verified that CAR-T cells can effectively deliver Ova peptide, we next tested 19BBz CAR-T cells that co-express SIINFEKL and RN7SL1 and assessed its efficacy against a low mutational burden tumor model for CAR antigen loss (Fig. 7I). For this, we implanted mice with tumors comprised of a 1:1 mix of human CD19^{+} and CD19^{-} KP lung cancer cells (DuPage et al., 2011) and adoptively transferred 5×10^{5} OT-I T cells to control for the presence of a pre-existing T cell pool. 19BBz CAR-T cells or 19BBz CAR-T cells that deliver either SIINFEKL or RN7SL1 has little effect. This suggests that in a poorly immunogenic heterogenous tumor, autonomous CAR function, recruitment of endogenous immunity, or provision of neoantigen without enhancing adjuvanticity are all individually insufficient. However, combining these functions by simultaneous CAR-T cell delivery of RN7SL1 plus SIINFEKL significantly delays tumor growth. Thus, these data suggest that multi-armored CAR-T cells can co-deploy peptide antigens with RN7SL1 to further recruit endogenous immunity, making CAR-T cells less susceptible to CAR antigen loss even if tumors with heterogenous CAR antigen expression lack adequate neoantigens.

DISCUSSION

Many strategies to improve CAR-T cells have focused on augmenting intrinsic functions to overcome therapeutic barriers such as low CAR antigen density or CAR antigen loss, both of which may be particularly relevant for solid tumors. Such strategies include designing CARs

with improved antigen affinity or with multiple specificities (Hamieh et al., 2019; Majzner et al., 2020). In this study, we address this problem by arming CAR-T cells with the ability to activate an endogenous immune response capable of rejecting CAR antigen-negative tumors, while also enhancing cell-intrinsic function (Fig. 7J). To achieve this, we engineered CAR-T cells to produce EVs containing RN7SL1, which functions as a DAMP to activate RNA PRRs. Within CAR-T cells, IFN signaling is overtly activated. This leads to greater CAR-T cell expansion and functionality, which is consistent with recent findings showing favorable effects of PRR activation in T cells (Li et al., 2020). In the TME, the delivery of RN7SL1 by CAR-T cell EVs is biased toward intratumoral immune cells, thereby mitigating PRR activation in cancer cells that can lead to immunosuppression and tumor progression. Within the myeloid and DC compartment, RN7SL1 engenders stimulatory features needed to effectively recruit endogenous T cells. When endogenous immunity is unleased with the aid of ICB, the resulting expansion of effector-memory-like CD8 T cells then contributes to anti-tumor immunity and protection against CAR antigen loss. Importantly, the ability of RN7SL1 to enhance endogenous immunity can now be combined with co-delivery of peptide antigens by CAR-T cells to “paint” poorly immunogenic tumors. Thus, arming CAR-T cells with RN7SL1 enhances autonomous function, recruits innate and adaptive endogenous immunity, and enables effective co-delivery of additional cargo to improve treatment of solid tumors.

In addition to the activation of IFN signaling in immune cells, the degree to which PRRs are activated in cancer cells relative to immune cells can have important consequences on tumor progression and response to immunotherapy. Specifically, in the absence of CD8 T cells, our current (Fig. 1B) and previous findings (Boelens et al., 2014; Nabet et al., 2017) suggest that RIG-I activation by RN7SL1 in cancer cells can promote tumor progression. Similar detrimental effects can occur when cGAS/STING is stimulated in cancer cells (Bakhoum et al., 2018; Chen et al., 2016). We add to this list by showing that in immunocompetent mice, RIG-I activation in cancer cells also contributes to suboptimal anti-tumor immune responses after ICB. This is likely due, at least in part, to an increase in cancer cell IFN-I signaling that is locally concentrated to cancer cells where it can drive expression of multiple immune inhibitory genes (Benci et al., 2019; Benci et al., 2016; Chen et al., 2019; Jacquelot et al., 2019). Thus, these collective observations suggest that PRR/IFN signaling can promote competing processes in cancer versus immune cells that ultimately impact the efficacy of immunotherapy. Delivering agonists selectively to the immune compartment generates productive IFN signaling that fosters anti-tumor immunity while limiting tumor progression.

Besides demonstrating that CAR-T cells can be used to preferentially deliver RN7SL1 to immune cells, our study highlights that differences in signaling properties of PRR agonists are also critical. Although RN7SL1 and Scr RNA can both stimulate IFN signaling *in vitro* and *in vivo*, our data indicate that only RN7SL1 can support productive endogenous immune activation and improve CAR-T cell-mediated tumor control. One intriguing difference between RN7SL1 and Scr RNA is that RN7SL1 requires both RIG-I and MDA5 to induce MHC-I and PDL1, while the Scr RNA only requires RIG-I. This suggests that RN7SL1 is tuned to activate PRRs more modestly compared to other agonists and might need to directly or indirectly activate both RNA sensors for robust signal amplification. Indeed, lower magnitude of PRR signaling has been shown to favor anti-tumor immunity (Sivick

et al., 2018) and the ability to activate both RIG-I and MDA5 *in vivo* may be critical to generate effective immunity in some cases (Stone et al., 2019). Thus, simply activating IFN signaling is likely insufficient for a PRR agonist to improve CAR-T cell function, which has implications for other immunotherapies as well.

We demonstrate that RN7SL1 and peptide antigens generated by CAR-T cells are delivered by extracellular vesicles and transferred to immune cells. T cells have been reported to secrete exosomes that can transfer RNA to antigen presenting cells (Mittelbrunn et al., 2011) or to use EVs to coordinate signaling across the immunological synapse (Choudhuri et al., 2014). Notably, our data suggest that EV-mediated transfer by CAR-T cells involves CAR engagement. Since CAR engagement results in killing of cancer cells, this may contribute to seemingly less transfer of EV RNA to cancer cells compared to immune cells; however, additional complexity is likely given that peptide transfer appears non-selective. Regardless, the coupling of EV-mediated payload delivery by CAR-T cells with CAR engagement may offer multiple advantages over other therapeutic delivery methods. For example, delivery of potent PRR agonists by CAR-T cells may effectively increase local therapeutic concentrations and generate a steady production of agonist across therapeutically relevant on-target sites, as has been shown in other contexts (Roybal et al., 2016). CAR-T cell delivery of RN7SL1 may also ensure proper timing of IFN signaling in DCs with tumor cell death, a coordination that can be important in achieving effective adaptive immunity (Tzeng et al., 2016). In contrast, PRR agonists given as intratumoral injections (Hammerich et al., 2019) or administered systemically (Ramanjulu et al., 2018) may be more difficult to correctly time for optimal immune activation or can suffer from limited pharmacological distribution and off-target effects (Hu et al., 2019).

Most human cancers lack adequate neoantigens, potentially limiting the benefit of CAR-T cells that can recruit an endogenous immune response. A major implication from our study is that CAR-T cells can be used to deliver RN7SL1 with a peptide antigen of choice. It is conceivable that a variety of shared antigens such as “hotspot” mutations to tumor suppressor genes or oncogenes (Klebanoff and Wolchok, 2018; Malekzadeh et al., 2019) could be targeted using this strategy. In addition, it may be possible to deliver peptides encoding one or more antigens to the TME, thereby recruiting a broad endogenous immune repertoire. Thus, CAR-T cells that deliver immunogenic DAMPs could be armored with multiple peptide antigens and possibly other peptide therapeutics to potentially overcome major barriers impeding CAR-T cell efficacy in solid tumors.

LIMITATIONS OF THE STUDY

Our work necessarily uses syngeneic mouse models to study how CAR-T cells that deliver EVs with RN7SL1 can recruit an endogenous anti-tumor immune response. Although human CAR-T cells in NSG mice are used to examine the impact of RN7SL1 on autonomous CAR-T cell function, the efficacy of RN7SL1 in recruiting endogenous anti-tumor immunity in humans or a humanized model needs to be determined. Future studies will also need to examine the scope of peptide antigens and cargo that can be effectively delivered by RN7SL1 CAR-T cells.

STAR METHODS

RESOURCE AVAILIBILITY

Lead contact.—Further information and requests for reagents may be directed to and will be fulfilled by the lead contact, Andy Minn (andyminn@upenn.edu).

Materials availability.—Plasmids generated in this study will be provided by the lead contact under a material transfer agreement.

Data and code availability.

- Single-cell RNA-seq data have been deposited at the GEO and are publicly available as of the date of publication. Accession numbers are listed in the key resources table.
- This paper does not report original code.
- Any additional information required to reanalyze the data reported in this paper is available from the lead contact upon request.

EXPERIMENTAL MODEL AND SUBJECT DETAILS

Mice.—All animal experiments were performed according to protocols approved by the Institutional Animal Care and Use Committee of the University of Pennsylvania. Five to eight week-old C57BL/6 (stock# 027) and CD45.1 (B6.SJL-Ptprc^{a} Pepc^{b}/BoyCrl, stock# 494) were obtained from Charles River Laboratory. Alternatively, five to seven-week-old female C57BL/6 (stock# 000664), and CD45.1 (B6.SJL-Ptprc^{a} Pepc^{b}/BoyCr, stock# 002014) were obtained from Jackson Laboratories in knockout studies. In these studies, *Batf3* KO (B6.129S(C)-*Batf3*^{tm1Kmm}/J; stock# 013755), *Tcra* KO (B6.129S2-*Tcra*^{tm1Mom}/J; stock# 002116), and *Mavs* KO (B6.129-*Mavs*^{tm1Zjc}/J; stock# 008634) were also from Jackson Laboratory (Bar Harbor, ME). Additionally, *Rig-I* (*Ddx58*) KO heterozygous mice (C57BL/6NJ-*Ddx58*$^{em1(IMPC)J}$/Mmjax; stock# 46070-JAX) were procured from Jackson Laboratories and bred at University of Pennsylvania. Littermate controls were used in this instance. Mice were maintained under pathogen free conditions.

Cell lines.—B16-F10 melanoma cells were purchased from ATCC and cultured as described (Twyman-Saint Victor et al., 2015). The *Kras*$^{LSL\text{-}G12D/+}$;*p53*$^{flox/flox}$ (KP) lung cancer cell line was a kind gift from Dr. David Feldser (Walter et al., 2019). CD19-expressing cell lines were stably transduced with pCLPs lentivirus encoding a truncated human CD19 antigen that is expressed on the cell surface but is unable to drive intracellular signaling. Cells were double sorted for stable expression. TC1-hMSLN lung cancer cell line was a kind gift from Dr. Steven Albelda (Moon et al., 2018).

METHOD DETAILS

Production of *in vitro* transcribed RNA.—*In vitro* transcription (IVT) was performed using of PCR amplified cDNA templates that contained Hepatitis Delta Virus Ribozyme to ensure homogeneous 3′ ends of the transcripts of interest. In vitro transcription was completed with the MEGAshortscript T7 Transcription Kit (ThermoFisher) per

manufacturer's instructions. RNA was DNase treated and phenol/chloroform purified. After thermocycling to ensure ribozyme cleavage, correct size transcripts were gel purified (Nabet et al., 2017). RNA secondary structure of RN7SL1 and scramble were predicted using RNAstructure (Reuter and Mathews, 2010).

***In vivo* mouse RNA studies.—**Tumor injection and treatment schedule were performed as previously described (Twyman-Saint Victor et al., 2015). In all cases, a single flank was implanted. Blocking antibodies against CTLA4 (9H10) and PD1 (RMP1–14) were administered intraperitoneally at 200 ug/dose, and were given on days 8, 11, and 14 unless otherwise specified. Anti-CD8 (2.43) and anti-CD4 (GK1.5) depleting antibodies were given on days −2, 0, 4, 8, 12, 16, and 20. Isotype controls were used to confirm the lack of non-specific effects and a similar survival response to untreated mice. RNA was packaged in liposomes (RNAiMax, Invitrogen) at 200 ng/mouse and injected on days 5, 8, and 11 unless otherwise specified.

Human chimeric antigen receptor T cells.—2×10^6 ASCP-1 tumor cells in log phase growth were implanted into flanks of NSG mice and allowed to reach a volume of ~200mm^3 (approximately 4 weeks). Mice were then treated with 1×10^6 mesothelin-specific human CAR-T cells. CAR-T cells were produced as previously described (Posey et al., 2016). Briefly, healthy donor T cells were stimulated with CD3/CD28 Dynabeads (Invitrogen) in the presence of 5 ng/mL IL7/IL15 for 24 hours, and then transduced with pTRPE-M5BBz lentivirus or variants thereof. 96 hours after transduction, beads were removed from culture and cells were allowed to rest down to a volume ~325 fL before cryopreservation. CAR-expressing T cells were quantified and characterized by anti-Fab(2)' staining and flow cytometry before i.v. tail vein injection. Extracellular vesicles were isolated from T cell expansion media prior to cryopreservation and were collected by serial high speed ultracentrifugation as previously described (Thery et al., 2006).

Murine chimeric antigen receptor T cells.—5×10^4 (B16-h19), 1×10^5 (KP-h19), or 2.5×10^5 (TC1-hMSLN) tumor cells in log phase growth were implanted into flanks of B6 mice and treated with murine CAR T cells at days 5 and 12. Murine T cells (WT or *Pmel*-transgenic) were stimulated with CD3/CD28 Dynabeads (Invitrogen) for 24 hours, and then transduced with pMSGV-h19BBz or pMSGV-M5BBz retrovirus or variants thereof. 48 hours after transduction, CAR-expressing T cells were quantified by anti-idiotype (19BBz) or anti-Fab(2)' (M5BBz) staining and flow cytometry. $1–5\times10^6$ CAR-expressing T cells were injected i.v. in mice bearing $hCD19^+$ tumors. Extracellular vesicles were isolated from T cell expansion media collected by serial high speed ultracentrifugation as described above. For IFNAR-blocking studies, mice were injected with 200 ug/dose of anti-IFNAR blocking antibody (MAR1–5A3) or PBS control intraperitoneally 24 hours prior to CAR-T treatment. Additional blocking antibody injections were administered every 4 days until mice reached experimental endpoints. In survival experiments, mice were treated with ICB antibodies anti-CTLA4 (9H10) and anti-PD1 (RMP1–14) intraperitoneally at 200 ug/dose on days 8, 11, and 14.

Bone marrow chimeras.—CD45.1$^+$ B6 mice were lethally irradiated at a dose of 9 Gy on day 0. 24 hours later (day 1), bone marrow was harvested by flushing the hindlimbs harvested from CD45.2$^+$ *Rig-I*$^{-/-}$ or WT littermate controls. Following RBC lysing by incubation with ACK, single cell suspensions were prepared, and 5×10^6 bone marrow cells were administered intravenously. Mice were allowed to reconstitute for 8 weeks. Prior to experimental use, CD45.2$^+$ reconstitution was verified by flow cytometry of PBMCs isolated by submandibular bleed. Tumors and CAR-T cells were administered as described above.

Flow cytometry.—Tumors were harvested at day 13–17 post tumor implantation. Peripheral blood samples were isolated at time points specified by submandibular bleed into heparin solution. Single-cell suspensions were prepared, and red blood cells were lysed using ACK Lysis Buffer (Life Technologies). For in vitro cell lines, sub-confluent cells were treated with 100 ng/mL of RNA or control liposome formulations and harvested 48 hours later. Single-cell suspensions were then prepared for antibody staining. Live/dead cell discrimination was performed using Live/Dead Fixable Aqua Dead Cell Stain Kit (Life Technologies). Cell surface staining was done for 30 min at 4 degrees. Intracellular staining was done using a fixation/permeabilization kit (eBioscience). Data acquisition was done using an LSR II (BD) and analysis was performed using FlowJo (TreeStar) or the R language and environment for statistical computing. For quantitation of immune infiltration, tumors were harvested and weighed. Subsequently, the entire tumor section was dissociated and stained. All events were collected on a flow cytometer and the total number of events for a given immune cell type were divided by the total cell number acquired.

RNA labeling of CAR-T cells.—T cells were expanded and transduced as described above. Before injection or in vitro culture, cells were labeled for 20 min with Syto RNASelect reagent (Invitrogen) at 37^o C in PBS. For *in vivo* experiments, cells were washed twice and injected intratumorally into flank tumors on day 14, and then harvested 24 hours later (day 15). For *in vitro* experiments, T cells were washed twice and then cultured *in vitro* with donor-matched PBMCs. RNA transfer was measured by flow cytometry using the 515/25 blue channel. In indicated cases, cells were treated with 1 uM GW4869 or DMSO for 24 hours before injection. Drug was washed out before RNA labeling and cell injection.

CRISPR gene targeting.—Gene targeting of RIG-I and MDA5 (IFIH1) by CRISPR/Cas9 was accomplished by transient transfection of the sgRNA oligo cloned into PX459 (Addgene) digested with BbsI (NEB) as per the manufacturer's instructions. The sgRNA-cloned PX459 plasmid was transfected using Lipofectamine 2000 at a ratio of 4 ug PX459 plasmid per 16 uL Lipofectamine 2000. After 24 hours of transfection, cells were selected in puromycin (1 ug/mL) for 48 hours, then plated for single-cell clones in 96-well plates. Successful targeting of the gene(s) of interest was determined by both western blotting for the proteins of interest (CST clone D74E4 for MDA5, and CST Clone D14G6 for RIG-I) following treatment with 1000 units/mL IFN-beta (PBL Assay Science) and also by functional loss of response to poly I:C transfection (LMW poly I:C for RIG-I, HMW poly I:C for MDA-5) via RT-qPCR and/or flow cytometry. sgRNA sequences are as follows:

Ifih1 sgRNA_1: CACCTGTGGTAACACCAGCG

Ifih1 sgRNA_2: GGAAACAGCGGGAATGAGTC

Ddx58 sgRNA_1: 1CGTTGGAGATGCTAAGACCG

Ddx58 sgRNA_2: TCCGCCAGAGATGAACGAAG

BMDC and OT-I CD8 T cell co-culture.—BMDC of indicated genotypes were prepared by flushing bone marrow from mouse hindlimbs and plating 1×10^5 cells/mL in RPMI media + 10% FBS and 30 ng/mL of mGM-CSF. Media was changed at day 4 of culture while retaining non-adherent cells. BMDC were stimulated with 100 ng/mL of IVT RNA or 50 ng/mL of EV-RNA at day 4. Vesicle-encapsulated RNA was prepared using serum-free OptiMEM media and RNAiMax reagent. On day 6, BMDC were harvested and loaded with 1 ug/mL SIINFEKL Ova peptide in serum-free PBS at 37° C for 2 hours. BMDC were then washed three times to remove excess peptide and residual RNA followed by resuspension in RPMI + 10% FBS. OT-I T cells were harvested from spleens of OT-I mice by CD8 T cell enrichment kit (StemCell) and then cultured with peptide-loaded BMDCs at a 1:1 ratio in 12-well plates. In indicated experiments, anti-IFNAR blocking antibody (MAR1–5A3) was added to cultures at the time of T cell co-culture at a concentration of 10 ug/mL.

qRT-PCR gene expression analysis.—Relative gene expression levels after qRT-PCR were defined using either ΔCt or the ΔΔCt method and normalizing to GAPDH (cellular RNA) or 18S (EV RNA). Human-specific RN7SL1 primers were designed to target a 3 bp difference between the mouse and human genes at the 3' primer terminus.

B16 tumor rechallenge.—C57BL/6 mice were implanted with 5×10^4 tumor cells mixed at a 1:1 ratio of B16-h19 and B16-F10 WT cells. Mice were then treated with CAR-T cell plus ICB regimen as described above. On day 80, mice that had achieved complete responses following treatment with 19BBz-7SL CAR-T cells were challenged with 5×10^4 B16-F10 WT tumor cells and tumor relapse was monitored. Naïve mice were challenged as control. Mice were sacrificed at endpoints described above.

Single-cell RNA-sequencing preparation.—B16 or ASPC1 tumors were harvested and processed into single cell suspensions. For B16 endogenous immune cell studies, viable $CD45.2^+$ cells were FACS sorted on an Aria II. For human CAR-T studies, viable $CD3^+$ events were FACS sorted for T cell enrichment. Single-cell emulsions were obtained using the 10x Genomics Controller and the v3 (B16) or v3.1 (ASPC1) Library and Gel Bead kit (10X Genomics). RNA-sequencing libraries were prepared as instructed by the 10X 3' kit protocol. Resulting libraries were sequenced on an Illumina NextSeq using a NextSeq 500/550 v2.5 High Output Kit.

QUANTIFICATION AND STATISTICAL ANALYSIS

Analysis of tumor growth, survival, and group differences.—Mice were randomly assigned a treatment group and tumor volume determined by caliper measurements. Differences in survival were determined for each group by the Kaplan-Meier method and the overall p-value was calculated by the log-rank or Wilcoxon test (in cases where proportional hazards assumption might be violated) using the *survival* R package. For mouse studies, an

event was defined as death or when tumor burden reached a pre-specified size to minimize morbidity. A mixed effect linear model using the *lmerTest* (v3.1.0) R package was used to determine differences in tumor growth curves. The significance of two-way comparisons was determined by two-sample, two-tailed t-test for parametric data and by a Wilcoxon test for non-parametric data. A Shapiro test was used to assist in determining normality. To assess the impact of treatment or genotype condition, multivariable linear regression was used to determine the significance of main and interaction effects.

Single-cell RNA-sequencing analysis and clustering.—*CellRanger* pipeline (10X Genomics) was used to process raw data. Here, BCL files were converted to FASTQ, reads were aligned to mouse (cellranger-mm10–3.0.0) or human (cellranger-hg-19–2.1) genomes and counted, biological replicates were aggregated, and sparse matrices were converted to dense matrices. Genes that were expressed in less than 0.1% cells were removed, and gene expression was denoised using *SAVER* (v1.1.2), (Huang et al., 2018). Additional filtering was carried out including genes expressed in less than 1% cells and cells with less than 500 detected genes. Cells with over 10% mitochondrial reads were removed, variations in UMI count, percent of mitochondrial contamination and cell cycle were regressed out, and conditions were integrated using *Seurat* (v3.1.2), (Stuart et al., 2019). Shared nearest neighbor (SNN) was used for clustering, and the cell type identities of the clusters were determined by examining expression of known markers and by gene set enrichment, as described below.

Cell trajectory and state analysis.—Cell trajectory analysis was carried out with *Monocle* (v2.12.0), (Qiu et al., 2017) using SAVER-denoised scRNA-seq data subsetted on either myeloid or CD8 T cells. For the ordering genes, we used differentially expressed genes (DEGs) from the SNN clusters and removed the proliferation-associated genes *Mki67*, *Top2a*, *Cdk1*, and *Cdk2*.

Immune cell cluster and state assignment.—To assign SNN clusters or Monocle cell states to an immune cell type, gene sets for various mouse immune cells were used to determine gene set enrichment scores. For general immune cell types, dendritic cell subsets, and myeloid cell subsets, previously published gene sets were used (Alshetaiwi et al., 2020; Zilionis et al., 2019), excluding genes with a log2 fold-change less than 0.5 compared to genes in other like gene sets. A core T cell exhaustion gene set was derived using an RNA-seq data set for CD8 T cells from LCMV infection (Hudson et al., 2019). Here, we extracted DEGs using *limma* (v3.40.6), (Ritchie et al., 2015), by comparing $CD101^{-}$ $TIM3^{-}$, $CD101^{-}$ $TIM3^{+}$, and $CD101^{+}$ $TIM3^{+}$ $PD\text{-}1^{+}$ CD8 T cells to naïve CD8 T cells and using a strict log2 fold-change greater than five and a false discovery rate (FDR) greater than 0.01. For the naïve gene set, a separate RNA-seq data set was used to extract DEGs expressed greater than two-fold in naïve CD8 T cells compared to terminal effector ($KLRG1^{hi}$ $CD127^{lo}$), memory precursor ($KLRG1^{lo}$ $CD127^{hi}$), central memory ($CD62L^{+}$), effector memory ($CD62L^{-}$), $PD1^{+}$ stem-like ($CXCR5^{+}$), and $PD1^{+}$ $TIM3^{+}$ exhausted CD8 T cells. Effector and effector-memory gene sets was derived by extracting genes that are expressed greater than two-fold in terminal effector or effector-memory cells compared to the other CD8 T cell subsets. For gene sets for exhausted CD8 T cell subsets, a third

RNA-seq data set was used (Beltra et al., 2020) to extract DEGS for Tex^{prog1} ($Ly108^{+}$ $CD69^{+}$), Tex^{prog2} ($Ly108^{+}$ $CD69^{-}$), Tex^{int} ($Ly108^{-}$ $CD69^{-}$) and Tex^{term} ($Ly108^{-}$ $CD69^{+}$) PD-1^{+} CD8 T cells using a log2 fold-change greater than 1.5 and FDR greater than 0.01. *GSVA* (v1.32.0) and default parameters was used to calculate gene set enrichment on the aggregated gene expression values for all cells in each cluster or state. Each cluster or state was then assigned to the immune cell type or subset with the greatest enrichment score.

Gene set enrichment and expression analysis.—Single-cell enrichment of gene sets was determined using *GSVA* (v1.32.0) (Hanzelmann et al., 2013) and default parameters for myeloid/DC and CD8 T cells. To compare enrichment scores of cells belonging to two groups, a two-sided Wilcoxon test was used. For analysis using all immune cells, gene expression values for all cells in each cluster were aggregated first for computational speed and a per cluster enrichment score was calculated. To estimate the significance of the enrichment scores, observed enrichment scores were compared to the distribution of scores from 1000 random gene sets. The Hallmark gene set for interferon-alpha was used as a gene set for type-one IFN ISGs. For the general MDSC gene set, shared differentially expressed genes between MDSCs and monocytes and between MDSCs and neutrophils with a log2 fold-change of at least 0.5 were used (Alshetaiwi et al., 2020). Gene sets for costimulatory genes (*Cd80*, *Cd86*, *Cd40*, *Relb*, *Cd83*) and immunomodulatory genes (*Cd274*, *Pdcd1lg2*, *Cd200*) expressed in dendritic cells were previously described (Maier et al., 2020).

Supplementary Material

Refer to Web version on PubMed Central for supplementary material.

ACKNOWLEDGMENTS

A.J.M. and D.Y. are supported by a program project grant from the NIH (1P01CA210944-01). A.J.M. and C.H.J. are supported by The Mark Foundation for Cancer Research and the Parker Institute for Cancer Immunotherapy. A.J.M. is also supported by the Breast Cancer Research Foundation. L.R.J. was supported by a fellowship from the NIH (F31CA228455). We thank the Feldser lab for sharing the KP cell line utilized throughout this study.

REFERENCES

Alshetaiwi H, Pervolarakis N, McIntyre LL, Ma D, Nguyen Q, Rath JA, Nee K, Hernandez G, Evans K, Torosian L, et al. (2020). Defining the emergence of myeloid-derived suppressor cells in breast cancer using single-cell transcriptomics. Sci Immunol 5.

Bakhoum SF, Ngo B, Laughney AM, Cavallo JA, Murphy CJ, Ly P, Shah P, Sriram RK, Watkins TBK, Taunk NK, et al. (2018). Chromosomal instability drives metastasis through a cytosolic DNA response. Nature 553, 467–472. [PubMed: 29342134]

Beltra JC, Manne S, Abdel-Hakeem MS, Kurachi M, Giles JR, Chen Z, Casella V, Ngiow SF, Khan O, Huang YJ, et al. (2020). Developmental Relationships of Four Exhausted CD8(+) T Cell Subsets Reveals Underlying Transcriptional and Epigenetic Landscape Control Mechanisms. Immunity.

Benci JL, Johnson LR, Choa R, Xu Y, Qiu J, Zhou Z, Xu B, Ye D, Nathanson KL, June CH, et al. (2019). Opposing Functions of Interferon Coordinate Adaptive and Innate Immune Responses to Cancer Immune Checkpoint Blockade. Cell 178, 933–948 e914. [PubMed: 31398344]

Benci JL, Xu B, Qiu Y, Wu TJ, Dada H, Twyman-Saint Victor C, Cucolo L, Lee DSM, Pauken KE, Huang AC, et al. (2016). Tumor Interferon Signaling Regulates a Multigenic Resistance Program to Immune Checkpoint Blockade. Cell 167, 1540–1554 e1512. [PubMed: 27912061]

Blanchard N, Lankar D, Faure F, Regnault A, Dumont C, Raposo G, and Hivroz C. (2002). TCR activation of human T cells induces the production of exosomes bearing the TCR/CD3/zeta complex. J Immunol 168, 3235–3241. [PubMed: 11907077]

Bloom MB, Perry-Lalley D, Robbins PF, Li Y, el-Gamil M, Rosenberg SA, and Yang JC (1997). Identification of tyrosinase-related protein 2 as a tumor rejection antigen for the B16 melanoma. J Exp Med 185, 453–459. [PubMed: 9053445]

Boelens MC, Wu TJ, Nabet BY, Xu B, Qiu Y, Yoon T, Azzam DJ, Twyman-Saint Victor C, Wiemann BZ, Ishwaran H, et al. (2014). Exosome transfer from stromal to breast cancer cells regulates therapy resistance pathways. Cell 159, 499–513. [PubMed: 25417103]

Catalano M, and O'Driscoll L. (2020). Inhibiting extracellular vesicles formation and release: a review of EV inhibitors. J Extracell Vesicles 9, 1703244.

Chen J, Cao Y, Markelc B, Kaeppler J, Vermeer JA, and Muschel RJ (2019). Type I IFN protects cancer cells from CD8+ T cell-mediated cytotoxicity after radiation. J Clin Invest 129, 4224–4238. [PubMed: 31483286]

Chen Q, Boire A, Jin X, Valiente M, Er EE, Lopez-Soto A, Jacob L, Patwa R, Shah H, Xu K, et al. (2016). Carcinoma-astrocyte gap junctions promote brain metastasis by cGAMP transfer. Nature 533, 493–498. [PubMed: 27225120]

Choudhuri K, Llodra J, Roth EW, Tsai J, Gordo S, Wucherpfennig KW, Kam LC, Stokes DL, and Dustin ML (2014). Polarized release of T-cell-receptor-enriched microvesicles at the immunological synapse. Nature 507, 118–123. [PubMed: 24487619]

Denks K, Vogt A, Sachelaru I, Petriman NA, Kudva R, and Koch HG (2014). The Sec translocon mediated protein transport in prokaryotes and eukaryotes. Mol Membr Biol 31, 58–84. [PubMed: 24762201]

DuPage M, Cheung AF, Mazumdar C, Winslow MM, Bronson R, Schmidt LM, Crowley D, Chen J, and Jacks T. (2011). Endogenous T cell responses to antigens expressed in lung adenocarcinomas delay malignant tumor progression. Cancer Cell 19, 72–85. [PubMed: 21251614]

Gardner R, Wu D, Cherian S, Fang M, Hanafi LA, Finney O, Smithers H, Jensen MC, Riddell SR, Maloney DG, et al. (2016). Acquisition of a CD19-negative myeloid phenotype allows immune escape of MLL-rearranged B-ALL from CD19 CAR-T-cell therapy. Blood 127, 2406–2410. [PubMed: 26907630]

Halic M, and Beckmann R. (2005). The signal recognition particle and its interactions during protein targeting. Curr Opin Struct Biol 15, 116–125. [PubMed: 15718142]

Hamieh M, Dobrin A, Cabriolu A, van der Stegen SJC, Giavridis T, Mansilla-Soto J, Eyquem J, Zhao Z, Whitlock BM, Miele MM, et al. (2019). CAR T cell trogocytosis and cooperative killing regulate tumour antigen escape. Nature 568, 112–116. [PubMed: 30918399]

Hammerich L, Marron TU, Upadhyay R, Svensson-Arvelund J, Dhainaut M, Hussein S, Zhan Y, Ostrowski D, Yellin M, Marsh H, et al. (2019). Systemic clinical tumor regressions and potentiation of PD1 blockade with in situ vaccination. Nat Med 25, 814–824. [PubMed: 30962585]

Hanzelmann S, Castelo R, and Guinney J. (2013). GSVA: gene set variation analysis for microarray and RNA-seq data. BMC Bioinformatics 14, 7. [PubMed: 23323831]

Hu Q, Ren H, Li G, Wang D, Zhou Q, Wu J, Zheng J, Huang J, Slade DA, Wu X, et al. (2019). STING-mediated intestinal barrier dysfunction contributes to lethal sepsis. EBioMedicine 41, 497–508. [PubMed: 30878597]

Huang M, Wang J, Torre E, Dueck H, Shaffer S, Bonasio R, Murray JI, Raj A, Li M, and Zhang NR (2018). SAVER: gene expression recovery for single-cell RNA sequencing. Nat Methods 15, 539–542. [PubMed: 29941873]

Hudson WH, Gensheimer J, Hashimoto M, Wieland A, Valanparambil RM, Li P, Lin JX, Konieczny BT, Im SJ, Freeman GJ, et al. (2019). Proliferating Transitory T Cells with an Effector-like Transcriptional Signature Emerge from PD-1(+) Stem-like CD8(+) T Cells during Chronic Infection. Immunity 51, 1043–1058 e1044. [PubMed: 31810882]

Hur S. (2019). Double-Stranded RNA Sensors and Modulators in Innate Immunity. Annu Rev Immunol 37, 349–375. [PubMed: 30673536]

Jacquelot N, Yamazaki T, Roberti MP, Duong CPM, Andrews MC, Verlingue L, Ferrere G, Becharef S, Vetizou M, Daillere R, et al. (2019). Sustained Type I interferon signaling as a mechanism of resistance to PD-1 blockade. Cell Res 29, 846–861. [PubMed: 31481761]

Kandasamy M, Suryawanshi A, Tundup S, Perez JT, Schmolke M, Manicassamy S, and Manicassamy B. (2016). RIG-I Signaling Is Critical for Efficient Polyfunctional T Cell Responses during Influenza Virus Infection. PLoS Pathog 12, e1005754.

Keskin DB, Anandappa AJ, Sun J, Tirosh I, Mathewson ND, Li S, Oliveira G, Giobbie-Hurder A, Felt K, Gjini E, et al. (2019). Neoantigen vaccine generates intratumoral T cell responses in phase Ib glioblastoma trial. Nature 565, 234–239. [PubMed: 30568305]

Klebanoff CA, and Wolchok JD (2018). Shared cancer neoantigens: Making private matters public. J Exp Med 215, 5–7. [PubMed: 29269561]

Kloss CC, Lee J, Zhang A, Chen F, Melenhorst JJ, Lacey SF, Maus MV, Fraietta JA, Zhao Y, and June CH (2018). Dominant-Negative TGF-beta Receptor Enhances PSMA-Targeted Human CAR T Cell Proliferation And Augments Prostate Cancer Eradication. Mol Ther 26, 1855–1866. [PubMed: 29807781]

Li W, Lu L, Lu J, Wang X, Yang C, Jin J, Wu L, Hong X, Li F, Cao D, et al. (2020). cGAS-STING-mediated DNA sensing maintains CD8(+) T cell stemness and promotes antitumor T cell therapy. Sci Transl Med 12.

Liu X, Ranganathan R, Jiang S, Fang C, Sun J, Kim S, Newick K, Lo A, June CH, Zhao Y, et al. (2016). A Chimeric Switch-Receptor Targeting PD1 Augments the Efficacy of Second-Generation CAR T Cells in Advanced Solid Tumors. Cancer Res 76, 1578–1590. [PubMed: 26979791]

MacDiarmid JA, Amaro-Mugridge NB, Madrid-Weiss J, Sedliarou I, Wetzel S, Kochar K, Brahmbhatt VN, Phillips L, Pattison ST, Petti C, et al. (2009). Sequential treatment of drug-resistant tumors with targeted minicells containing siRNA or a cytotoxic drug. Nat Biotechnol 27, 643–651. [PubMed: 19561595]

Maier B, Leader AM, Chen ST, Tung N, Chang C, LeBerichel J, Chudnovskiy A, Maskey S, Walker L, Finnigan JP, et al. (2020). A conserved dendritic-cell regulatory program limits antitumour immunity. Nature 580, 257–262. [PubMed: 32269339]

Majzner RG, and Mackall CL (2019). Clinical lessons learned from the first leg of the CAR T cell journey. Nat Med 25, 1341–1355. [PubMed: 31501612]

Majzner RG, Rietberg SP, Sotillo E, Dong R, Vachharajani VT, Labanieh L, Myklebust JH, Kadapakkam M, Weber EW, Tousley AM, et al. (2020). Tuning the Antigen Density Requirement for CAR T-cell Activity. Cancer Discov 10, 702–723. [PubMed: 32193224]

Malekzadeh P, Pasetto A, Robbins PF, Parkhurst MR, Paria BC, Jia L, Gartner JJ, Hill V, Yu Z, Restifo NP, et al. (2019). Neoantigen screening identifies broad TP53 mutant immunogenicity in patients with epithelial cancers. J Clin Invest 129, 1109–1114. [PubMed: 30714987]

Mittelbrunn M, Gutierrez-Vazquez C, Villarroya-Beltri C, Gonzalez S, Sanchez-Cabo F, Gonzalez MA, Bernad A, and Sanchez-Madrid F. (2011). Unidirectional transfer of microRNA-loaded exosomes from T cells to antigen-presenting cells. Nat Commun 2, 282. [PubMed: 21505438]

Moon EK, Wang LS, Bekdache K, Lynn RC, Lo A, Thorne SH, and Albelda SM (2018). Intra-tumoral delivery of CXCL11 via a vaccinia virus, but not by modified T cells, enhances the efficacy of adoptive T cell therapy and vaccines. Oncoimmunology 7, e1395997.

Nabet BY, Qiu Y, Shabason JE, Wu TJ, Yoon T, Kim BC, Benci JL, DeMichele AM, Tchou J, Marcotrigiano J, et al. (2017). Exosome RNA Unshielding Couples Stromal Activation to Pattern Recognition Receptor Signaling in Cancer. Cell 170, 352–366 e313. [PubMed: 28709002]

Porgador A, Yewdell JW, Deng Y, Bennink JR, and Germain RN (1997). Localization, quantitation, and in situ detection of specific peptide-MHC class I complexes using a monoclonal antibody. Immunity 6, 715–726. [PubMed: 9208844]

Posey AD Jr., Schwab RD, Boesteanu AC, Steentoft C, Mandel U, Engels B, Stone JD, Madsen TD, Schreiber K, Haines KM, et al. (2016). Engineered CAR T Cells Targeting the Cancer-Associated Tn-Glycoform of the Membrane Mucin MUC1 Control Adenocarcinoma. Immunity 44, 1444–1454. [PubMed: 27332733]

Qiu X, Mao Q, Tang Y, Wang L, Chawla R, Pliner HA, and Trapnell C. (2017). Reversed graph embedding resolves complex single-cell trajectories. Nat Methods 14, 979–982. [PubMed: 28825705]

Ramanjulu JM, Pesiridis GS, Yang J, Concha N, Singhaus R, Zhang SY, Tran JL, Moore P, Lehmann S, Eberl HC, et al. (2018). Design of amidobenzimidazole STING receptor agonists with systemic activity. Nature 564, 439–443. [PubMed: 30405246]

Reuter JS, and Mathews DH (2010). RNAstructure: software for RNA secondary structure prediction and analysis. BMC Bioinformatics 11, 129. [PubMed: 20230624]

Ritchie ME, Phipson B, Wu D, Hu Y, Law CW, Shi W, and Smyth GK (2015). limma powers differential expression analyses for RNA-sequencing and microarray studies. Nucleic Acids Res 43, e47. [PubMed: 25605792]

Roth TL, Li PJ, Blaeschke F, Nies JF, Apathy R, Mowery C, Yu R, Nguyen MLT, Lee Y, Truong A, et al. (2020). Pooled Knockin Targeting for Genome Engineering of Cellular Immunotherapies. Cell 181, 728–744 e721. [PubMed: 32302591]

Roybal KT, Williams JZ, Morsut L, Rupp LJ, Kolinko I, Choe JH, Walker WJ, McNally KA, and Lim WA (2016). Engineering T Cells with Customized Therapeutic Response Programs Using Synthetic Notch Receptors. Cell 167, 419–432 e416. [PubMed: 27693353]

Sivick KE, Desbien AL, Glickman LH, Reiner GL, Corrales L, Surh NH, Hudson TE, Vu UT, Francica BJ, Banda T, et al. (2018). Magnitude of Therapeutic STING Activation Determines CD8(+) T Cell-Mediated Anti-tumor Immunity. Cell Rep 25, 3074–3085 e3075. [PubMed: 30540940]

Sotillo E, Barrett DM, Black KL, Bagashev A, Oldridge D, Wu G, Sussman R, Lanauze C, Ruella M, Gazzara MR, et al. (2015). Convergence of Acquired Mutations and Alternative Splicing of CD19 Enables Resistance to CART-19 Immunotherapy. Cancer Discov 5, 1282–1295. [PubMed: 26516065]

Stone AEL, Green R, Wilkins C, Hemann EA, and Gale M Jr. (2019). RIG-I-like receptors direct inflammatory macrophage polarization against West Nile virus infection. Nat Commun 10, 3649. [PubMed: 31409781]

Stuart T, Butler A, Hoffman P, Hafemeister C, Papalexi E, Mauck WM 3rd, Hao Y, Stoeckius M, Smibert P, and Satija R. (2019). Comprehensive Integration of Single-Cell Data. Cell 177, 1888–1902 e1821. [PubMed: 31178118]

Tang N, Cheng C, Zhang X, Qiao M, Li N, Mu W, Wei XF, Han W, and Wang H. (2020). TGF-beta inhibition via CRISPR promotes the long-term efficacy of CAR T cells against solid tumors. JCI Insight 5.

Thery C, Amigorena S, Raposo G, and Clayton A. (2006). Isolation and characterization of exosomes from cell culture supernatants and biological fluids. Curr Protoc Cell Biol Chapter 3, Unit 3 22.

Twyman-Saint Victor C, Rech AJ, Maity A, Rengan R, Pauken KE, Stelekati E, Benci JL, Xu B, Dada H, Odorizzi PM, et al. (2015). Radiation and dual checkpoint blockade activate non-redundant immune mechanisms in cancer. Nature 520, 373–377. [PubMed: 25754329]

Tzeng A, Kauke MJ, Zhu EF, Moynihan KD, Opel CF, Yang NJ, Mehta N, Kelly RL, Szeto GL, Overwijk WW, et al. (2016). Temporally Programmed CD8alpha(+) DC Activation Enhances Combination Cancer Immunotherapy. Cell Rep 17, 2503–2511. [PubMed: 27926855]

Walter DM, Yates TJ, Ruiz-Torres M, Kim-Kiselak C, Gudiel AA, Deshpande C, Wang WZ, Cicchini M, Stokes KL, Tobias JW, et al. (2019). RB constrains lineage fidelity and multiple stages of tumour progression and metastasis. Nature 569, 423–427. [PubMed: 31043741]

Wu TD, Madireddi S, de Almeida PE, Banchereau R, Chen YJ, Chitre AS, Chiang EY, Iftikhar H, O'Gorman WE, Au-Yeung A, et al. (2020). Peripheral T cell expansion predicts tumour infiltration and clinical response. Nature 579, 274–278. [PubMed: 32103181]

Zilionis R, Engblom C, Pfirschke C, Savova V, Zemmour D, Saatcioglu HD, Krishnan I, Maroni G, Meyerovitz CV, Kerwin CM, et al. (2019). Single-Cell Transcriptomics of Human and Mouse Lung Cancers Reveals Conserved Myeloid Populations across Individuals and Species. Immunity 50, 1317–1334 e1310. [PubMed: 30979687]

HIGHLIGHTS

- CAR-T cells deliver RN7SL1 in extracellular vesicles (EVs) and activate RIG-I
- CAR-T cells expressing RN7SL1 exhibit greater expansion, persistence, and less exhaustion
- Preferential uptake of RN7SL1 by DC/myeloid over tumor cells enhances endogenous immunity
- CAR-T EVs can co-deliver antigen with RN7SL1 to reject tumors with CAR antigen loss

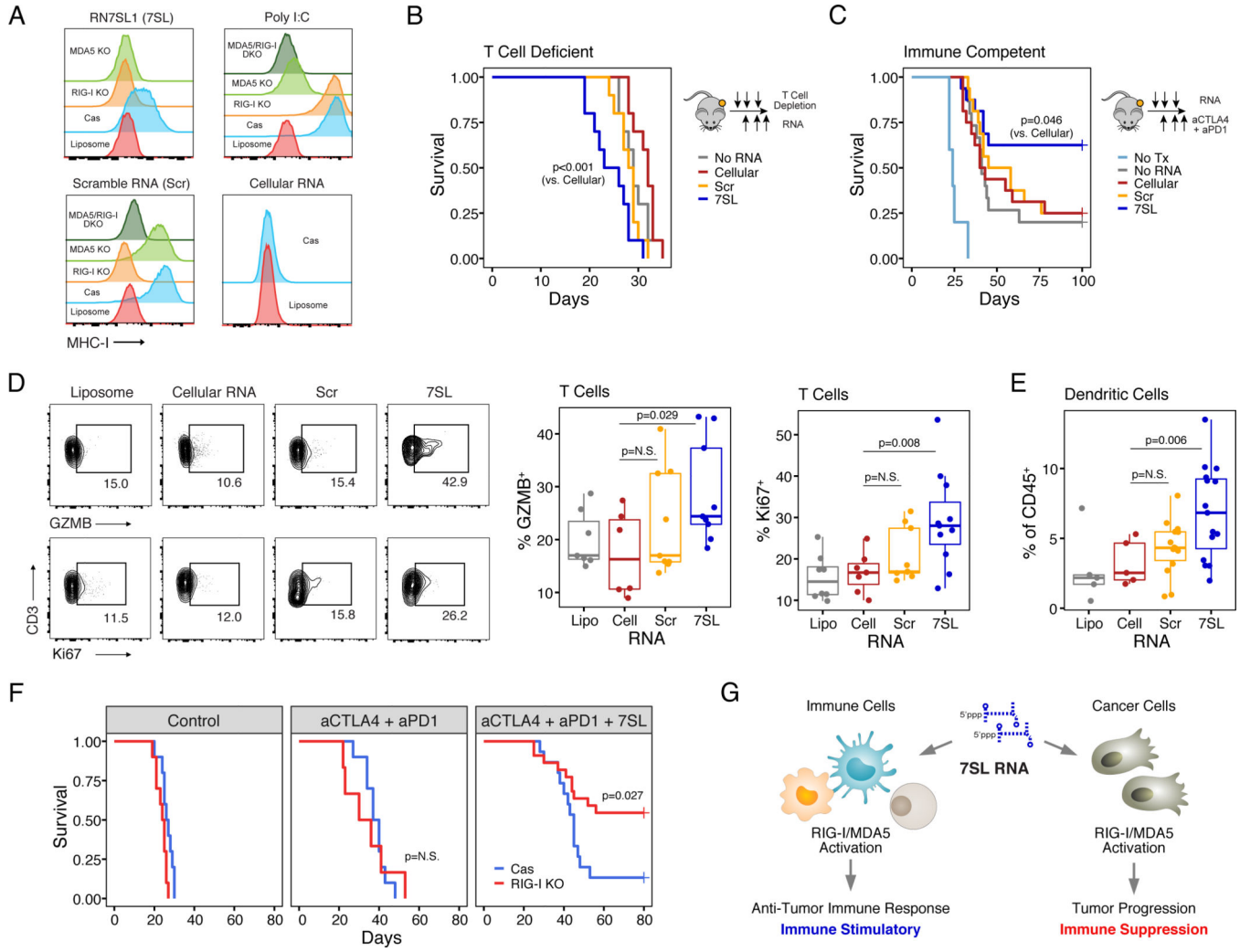

Figure 1. Sensing of RN7SL1 by immune cells rather than cancer cells favors anti-tumor immune responses.

A. MHC-I expression on B16-F10 with or without RIG-I and/or MDA5 knockout after transfection with RN7SL1 (7SL), Scr RNA (Scr), poly I:C, or cellular RNA. Expression on Cas9 control cells (Cas) and after liposome-only transfection are also shown.

B-C. Survival of mice bearing B16-F10 tumors after intratumoral injection of the indicated RNA on days 5, 8, and 11 combined with treatment with CD4 and CD8 T cell depleting antibodies (n=10 per group) **(B)** or treatment with anti-CTLA4 + anti-PD1 (n=15–16 per group) **(C)**.

D-E. GZMB and Ki67 expression in intratumoral $CD3^+$ T cells **(D)** or DC infiltration **(E)** from mice with B16-F10 tumors injected with the indicated RNA. Tumors were harvested at day 15.

F. Survival of mice with control or RIG-I knockout B16-F10 tumors after the indicated treatment (n=6–22 per group).

G. Model for how PRR signaling affects different cellular compartments within the TME.

P-values for survival are by log-rank test. For comparison between two groups, a two-sided T-test or Wilcoxon test is used for parametric or non-parametric data, respectively. See also Figure S1.

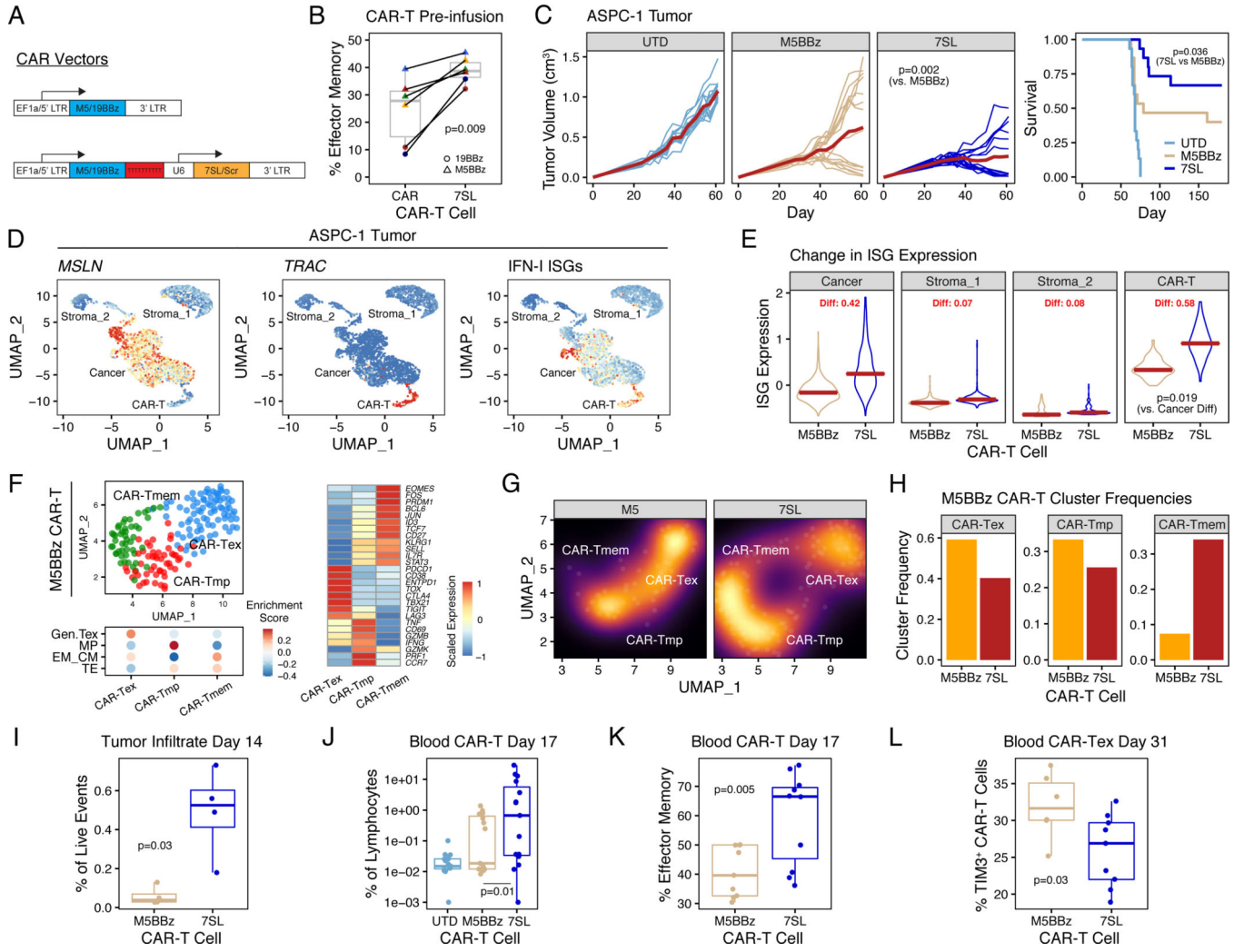

Figure 2. Human CAR-T cells engineered to express RN7SL1 enhance solid tumor control

A. Construct design for M5BBz (M5) and 19BBz CARs with and without co-expression of RN7SL1 (7SL) or Scr RNA. EF1a promoter is utilized for human CAR vectors and 5' LTR for mouse.

B. Effector-memory differentiation pre-infusion defined by $CCR7^{-}/CD45RO^{+}$ for the indicated CAR-T cells with or without RN7SL1 expression. Colors are independent donors.

C. Tumor growth and survival from NSG mice bearing ASPC-1 tumors treated with untransduced (UTD), M5BBz, or M5BBz-7SL (7SL) CAR-T cells. N=15 mice/group, 3 independent donors.

D. Cell populations in ASPC-1 tumors overlaid with expression for the indicated genes or an IFN-I ISG metagene (red is high expression and blue is low).

E. Distribution of IFN-I ISG metagene values for cells in the indicated populations shown in (D). Labeled in red text are differences in the median values (maroon line) between M5BBz-7SL and M5BBz CAR-T cell treated groups. The p-value shows the significance of this difference when comparing CAR-T and cancer cell populations.

F. M5BBz CAR-T cell subsets from (D) along with enrichment of gene sets for T cell exhaustion (Gen.Tex), memory precursor (MP), effector/central memory (EM_CM), or terminal effector (TE). Heatmap for select genes is also shown (right).
G-H. Density plot **(G)** and quantification **(H)** of frequencies for indicated CAR-T cell subsets. **I-J**. Frequency of CAR-T cells post-infusion in ASPC-1 tumors **(I)** or peripheral blood **(J)** as measured by flow cytometry.
K-L. $CCR7^{-}/CD45RO^{+}$ effector memory differentiation of CAR-T cells in peripheral blood **(K)** or CAR-T cell exhaustion measured using TIM3 **(L)**. N=5–15 mice/group, 3 independent donors. P-values for survival are by log-rank test. For comparison between two groups, a two-sided T-test or Wilcoxon test is used for parametric or non-parametric data, respectively. Mixed effect model is used for tumor growth analysis. See also Figure S2.

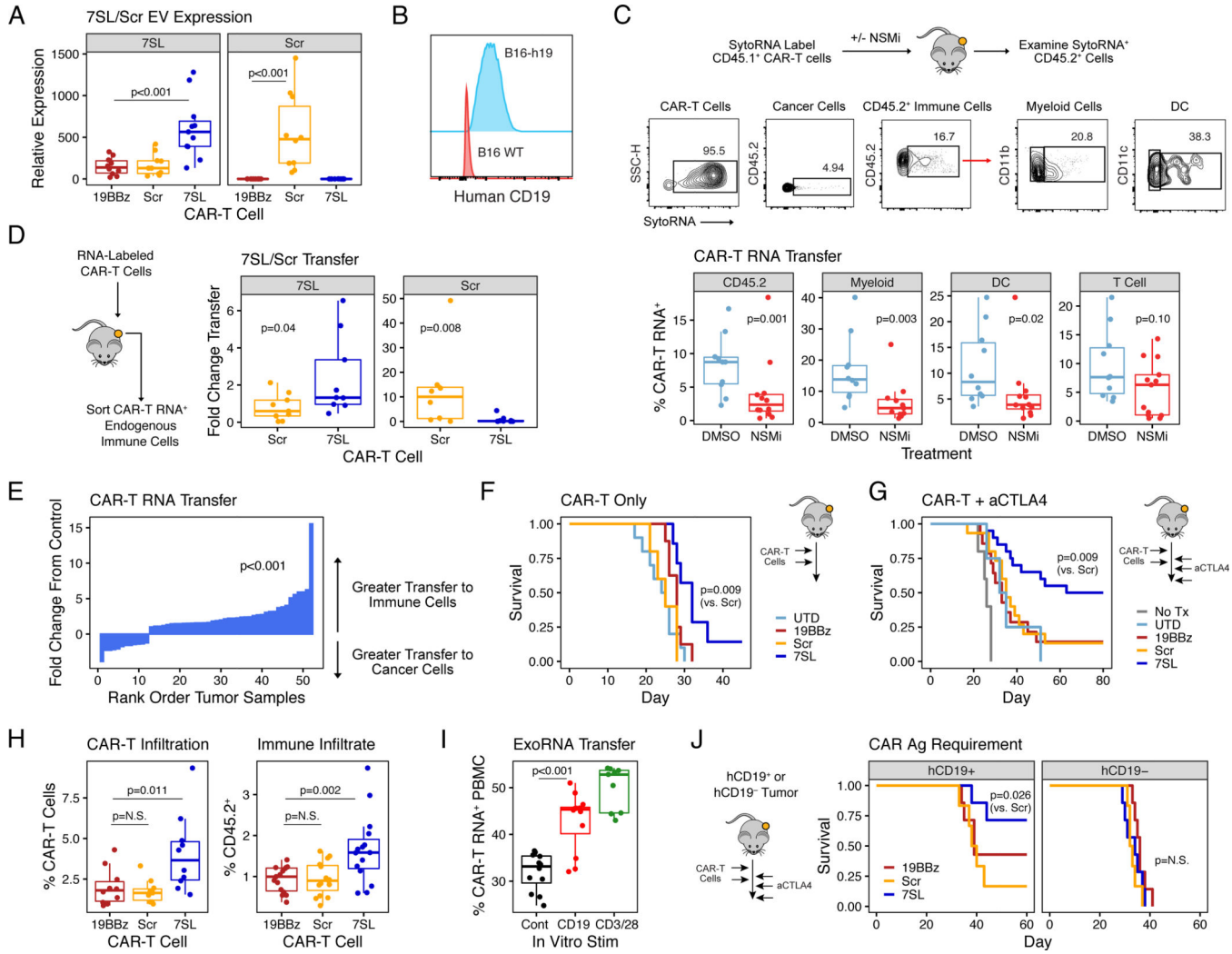

Figure 3. CAR-T cells deploying RN7SL1 in extracellular vesicles preferentially deliver RNA to endogenous immune cells and improve anti-tumor response.

A. Detection of RN7SL1 (7SL) or Scr RNA (Scr) from extracellular vesicles (EVs) secreted by mouse 19BBz CAR-T cells as assayed by qRT-PCR.

B. Ectopic expression of human CD19 on mouse B16 melanoma cells (B16-h19).

C. Transfer of RNA from CD45.1^{+} CAR-T cells to CD45.2^{-} cancer cells or CD45.2^{+} immune cells in B16-h19 tumors (top). Prior to RNA labeling with SytoRNA, CAR-T cells were treated with DMSO or a neutral sphingomyelinase inhibitor (NSMi) to block EV secretion and then transferred to tumor-bearing mice. RNA transfer was assessed 24 hours later.

D. Presence of 7SL or Scr from sorted intratumoral CD45.2^{+} immune cells positive for SytoRNA.

E. Relative transfer of CAR-T cell RNA to either CD45.2^{+} immune cells or CD45.2^{-} cancer cells quantified by flow cytometry of individual tumors. Fold change from equal transfer is shown. Positive and negative values indicate greater transfer to immune cells or cancer cells, respectively.

F-G. Survival of mice with B16-h19 tumors treated with 19BBz, 19BBz-7SL (7SL), 19BBz-Scr (Scr), or untransduced (UTD) CAR-T cells on days 5 and 12 (n=5–10 per group) **(F)** or combined with anti-CTLA4 on days 8, 11, and 14 (n=14–20 per group) **(G)**. No treatment (No Tx) group is also shown (n=5).

H. Frequency of transferred $CD45.1^+$ CAR-T cells or endogenous $CD45.2^+$ immune cells in B16-h19 tumors at day 15 after treatment. Frequencies are relative to live cells.

I. RNA transfer from human 19BBz-7SL CAR-T cells to donor-matched PBMCs following stimulation with the indicated beads.

J. Survival of mice bearing B16 tumors with or without human CD19 expression following treatment with indicated CAR-T cells (n=7–8 per group).

P-values for survival are by log-rank test. For comparison between two groups, a two-sided T-test or Wilcoxon test is used for parametric or non-parametric data, respectively. See also Figure S3.

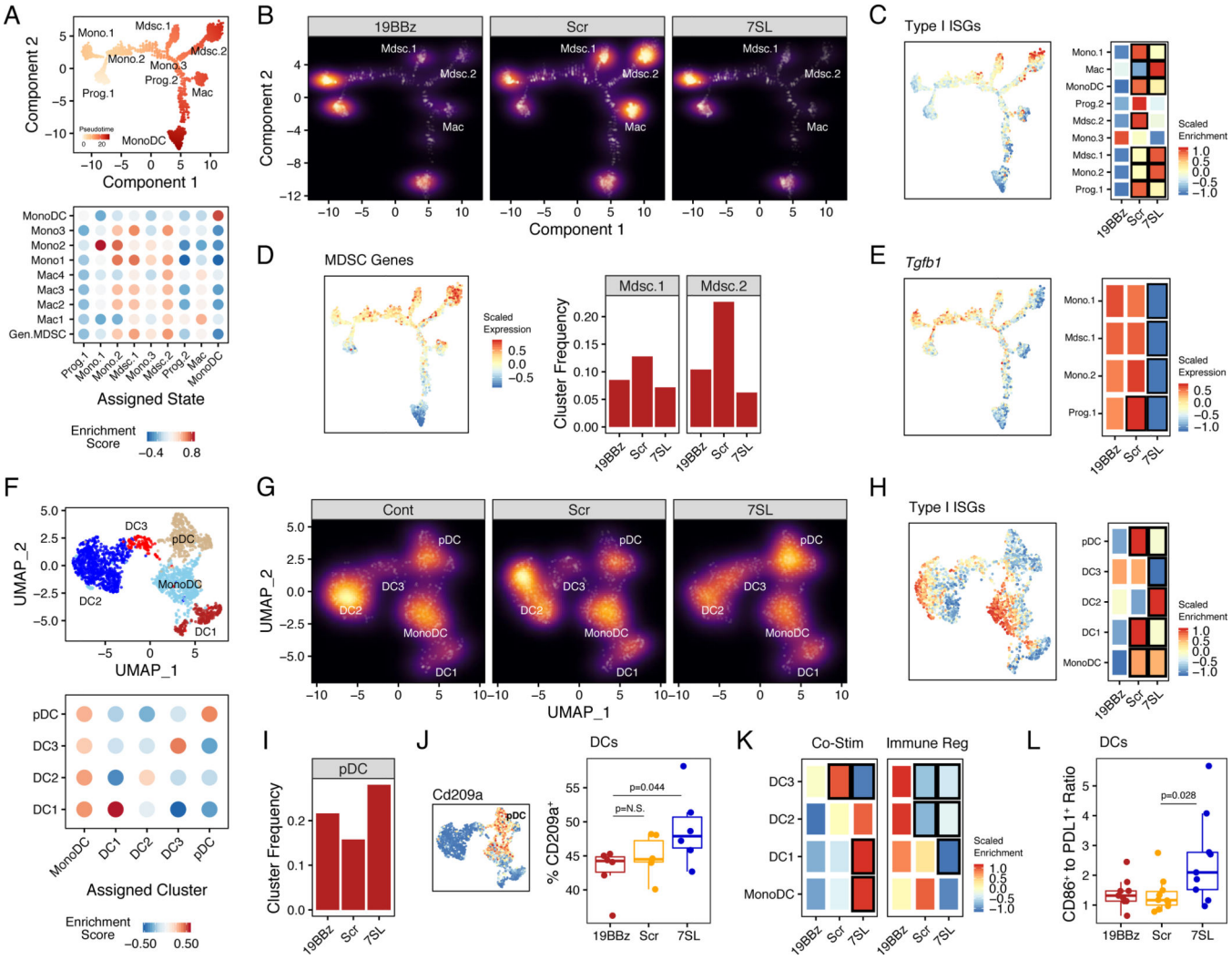

Figure 4. Deployment of RN7SL1 by CAR-T cells restricts suppressive features of myeloid cells and promotes co-stimulatory features of dendritic cells.

A. Differentiation trajectory and cell states for myeloid cells and DCs from B16-h19 tumors treated with CAR-T cells alone (top). Pseudotime values are color-coded. The identity of each state was determined by enrichment of gene sets (bottom) for monocytic (Mono), macrophage (Mac), or DC or monocytic DC (MonoDC) cell types. Also included is a gene set for MDSCs (Gen.MDSC).

B. Distribution of myeloid cells in each cell state after treatment with the indicated CAR-T cells. Shown are relative densities overlaid on the differentiation trajectory plot.

C. Enrichment scores for type I IFN-stimulated genes (ISGs) for each myeloid state and after treatment with the indicated CAR-T cells. Black boxes in the heatmap outline values with $p < 0.05$.

D. Average expression of MDSC genes for each myeloid state and the frequency of myeloid cells in each of the two states most enriched in MDSC genes.

E. Expression of *Tgfb1* for each myeloid state and after CAR-T cell therapy. Black boxes in the heatmap outline values with $p < 0.05$.

F. DC states from CD45.2$^+$ intratumoral immune cells from **(A)** were reclustered and shown on a UMAP plot (top). Clusters were assigned based on enrichment of gene sets for the indicated DC subtype (bottom).

G. Distribution of DC subtypes shown by relative densities overlaid on the UMAP plot.

H. Enrichment scores for ISGs for each DC subtype and after CAR-T cell therapy. Black boxes in the heatmap outline values with $p < 0.05$.

I-J. Frequency of pDC-like cells **(I)** and percentage of DCs expressing the pDC marker CD209a by flow cytometry after CAR-T cell therapy **(J)**.

K-L. Enrichment scores for co-stimulatory (left) and negative immunoregulatory (right) genes for each DC subtype **(K)**, and ratio of DCs expressing CD86 or PDL1 by flow cytometry **(L)** after CAR-T cell therapy. Black boxes in the heatmap outline values with $p < 0.05$.

For comparison between two groups, a two-sided T-test or Wilcoxon test is used for parametric or non-parametric data, respectively. See also Figure S4.

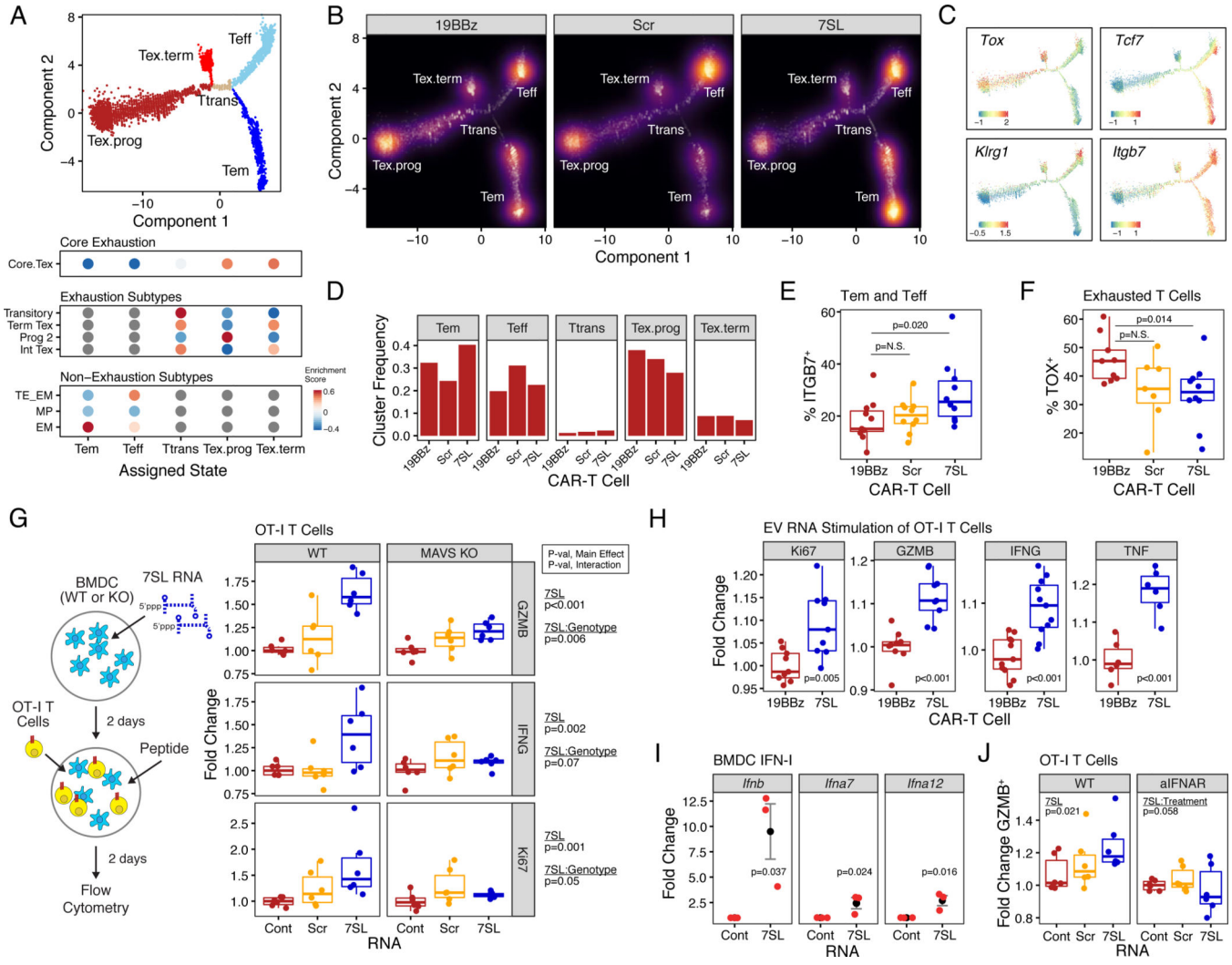

Figure 5. CAR-T cell delivery of RN7SL1 results in greater DC stimulation and expansion of endogenous effector-memory-like CD8 T cells.

A. Differentiation trajectory and cell states for CD45.2^{+} non-naïve CD8 T cells from B16-h19 tumors treated with CAR-T cells alone (top). The identity of each state was determined by enrichment of gene sets (bottom) for CD8 T cell exhaustion (Core.Tex) followed by gene sets for exhausted subsets (transitory, progenitor 2: Prog 2, intermediate: Int Tex, and terminal: Term Tex) or for non-exhausted subsets (memory precursor: MP, effector-memory: EM, terminal-effector/effector-memory: TE_EM).

B. Distribution of endogenous CD8 T cells in each cell state after treatment with indicated CAR-T cells. Relative densities are overlaid on the trajectory plot.

C. Expression of select marker genes associated with exhausted and non-exhausted CD8 T cells.

D. Frequency of CD8 T cells in each state after CAR-T cell therapy.

E-F. Percent of CD8 T cells expressing ITGB7 **(E)** or TOX **(F)** by flow cytometry.

G. Expression of the indicated markers on OT-I T cells after stimulation of BMDCs from wildtype or MAVS KO mice with RN7SL (7SL) or Scr RNA (Scr). Fold change is relative to

control liposomes (Cont). P-values for effect of 7SL and whether this effect is influenced by BMDC genotype (7SL:Genotype) are shown in the right-hand margin.

H. Increase in activation markers on OT-I T cells after BMDCs were stimulated with EV RNA from 19BBz or 19BBz-7SL (7SL) CAR-T cells.

I. Increase in type I IFN genes by qRT-PCR relative to liposome control (Cont) from BMDCs stimulated with 7SL.

J. Increase in OT-I T cells expressing GZMB after BMDC stimulation with the indicated RNA as described in **(G)** with or without anti-IFNAR antibody. Shown are P-values for effect of 7SL and whether this effect is influenced by anti-IFNAR treatment (7SL:Treatment).

For comparison between two groups, a two-sided T-test or Wilcoxon test is used for parametric or non-parametric data, respectively. Multivariable linear regression is used to determine significance of 7SL and interaction effects. See also Figure S5.

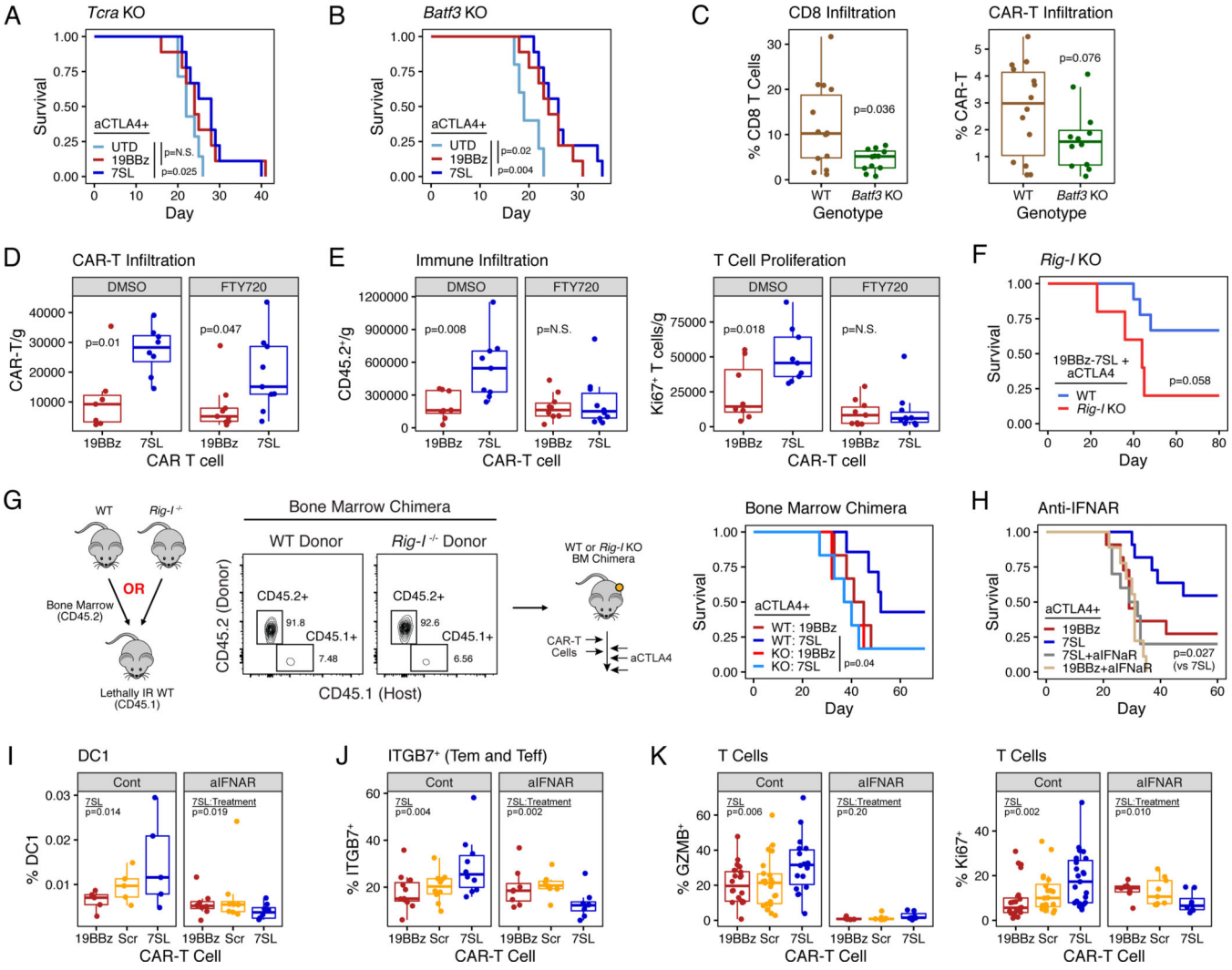

Figure 6. Endogenous T cells, dendritic cells, and activation of host RIG-I are required for RN7SL1 to enhance CAR-T cell response.

A-B. Survival of T cell-deficient *Tcra*$^{-/-}$ **(A)** or cDC1-deficient *Batf3*$^{-/-}$ **(B)** mice bearing B16-h19 tumors treated with indicated CAR-T cells plus anti-CTLA4 (aCTLA4) (n=7–9 per group).

C. Percentage of endogenous CD8 T cells (left) or CAR-T cells (right) in wildtype (WT) or *Batf3*$^{-/-}$ mice bearing B16-h19 tumors and treated with CAR-T cells.

D-E. Frequency of CAR-T cells **(D)** or endogenous immune cells **(E)** per gram of tumor following CAR-T cell therapy with or without FTY720. Contribution of Ki67^{+} T cells is separately shown **(E, right)**.

F-H. Survival of *Rig-I*$^{-/-}$ mice (n=5–9 per group) **(F)**, *Rig-I*$^{-/-}$ bone marrow chimera mice (n=6–7 per group) **(G)**, or anti-IFNAR (aIFNAR) treated wildtype mice (n=9–11 per group) **(H)** bearing B16-h19 tumors and treated with CAR-T cells plus anti-CTLA4. Flow plots in **(G)** show representative bone marrow reconstitution from WT or *Rig-I*$^{-/-}$ donor.

I-K. Percentage of intratmoral DC1 dendritic cells **(I)**, endogenous ITGB7^{+} effector-memory-like CD8^{+} T cells **(J)**, or endogenous T cells expressing GZMB or Ki67 **(K)**

after CAR-T cell therapy with or without anti-IFNAR. ITGB7^{+} T cell data from Fig. 5E is provided for reference. Shown are P-values for effect of 7SL and whether this effect is influenced by anti-IFNAR treatment (7SL:Treatment).

P-values for survival are by log-rank test. For comparison between two groups, a two-sided T-test or Wilcoxon test is used for parametric or non-parametric data, respectively. Multivariable linear regression is used to determine significance of 7SL and interaction effects. See also Figure S6.

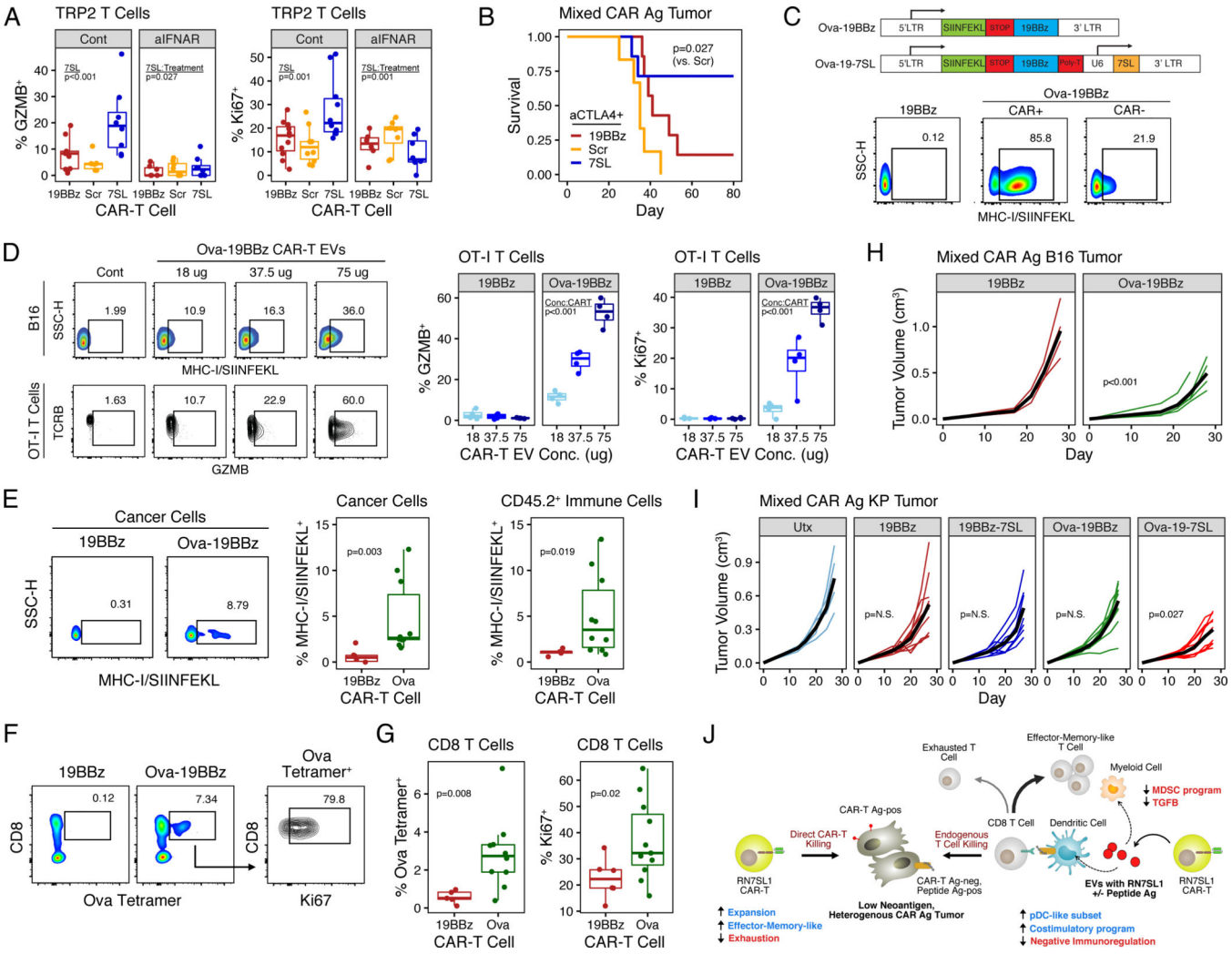

Figure 7. CAR-T cell deployment of RN7SL1 with peptide antigen overcomes resistance of poorly immunogenic tumors with heterogeneous CAR antigen expression.

A. Percentage of TRP2^{+} CD8 T cells from B16-h19 tumors expressing GZMB or Ki67 after CAR-T cell therapy. Shown are P-values for effect of 7SL and whether this effect is influenced by anti-IFNAR treatment (7SL:Treatment).

B. Survival after CAR-T cell therapy of mice bearing a heterogenous tumor comprised of a 1:1 mix of B16 cells with and without human CD19 (n=6–7 per group).

C. Design of 19BBz CAR vector expressing Ova (Ova-19BBz) or Ova plus RN7SL1 (Ova-19–7SL) (top) and representative flow cytometry plots showing detection of SIINFEKL peptide on CAR^{+} and CAR^{-} T cells (bottom).

D. Detection of SIINFEKL peptide on B16 cells loaded with indicated concentrations of EVs from Ova-19BBz CAR-T cells or 19BBz CAR-T cells (Cont) (flow plots, top). OT-I T cells were then added and activation was measured (flow plots, bottom) and quantitated (right) using GZMB and Ki67.

E. SIINFEKL peptide transfer to cancer and immune cells measured in mixed CD19^{+} and CD19^{-} B16 tumors following treatment *in vivo* with 19BBz or Ova-19BBz (Ova) CAR-T cells. Representative flow cytometry plots of cancer cells are shown (left).

F-G. Endogenous Ova-specific T cell expansion measured by tetramer and Ki67 expression **(F)**, and frequency of Ova-specific and Ki67-positive CD8 T cells **(G)**.

H. Growth of heterogenous $CD19^{+}/CD19^{-}$ B16 tumors following treatment with indicated CAR-T cells.

I. Growth of heterogenous $CD19^{+}/CD19^{-}$ KP mixed tumors following CAR-T cell therapy with anti-CTLA4 plus anti-PD1. 5×10^{5} OT-I T cells were transferred prior to tumor implantation.

J. Model for how CAR-T cells delivering RN7SL1 +/− peptide antigen improve solid tumor response.

P-values for survival are by log-rank test. Multivariable linear regression is used to determine significance of 7SL and interaction effects. Mixed effect model is used for tumor growth analysis. See also Figure S7.

key resources table

REAGENT or RESOURCE	SOURCE	DENTIFIER
Antbodies		
Ant-mouse CD3	Biolegend	Cat# 100204
Ant-mouse CD4	Invitrogen	Cat# 45-0042-82
Ant-mouse CD8	Invitrogen	Cat# 48-0081-82
Ant-human Tox	Miltenyi	Cat# 130-120-716
Ant-mouse CD45.2	Biolegend	Cat# 109822
Ant-mouse CD45.1	Biolegend	Cat# 110716
Ant-mouse Ki67	BD	Cat# 563755
Ant-mouse GzmB	Biolegend	Cat# GRB18
Ant-mouse CD69	Biolegend	Cat# 104541
Ant-mouse CD11b	BD	Cat# 553311
Ant-mouse F4/80	Biolegend	Cat# 123114
Ant-mouse CD11c	Biolegend	Cat# 100204
Ant-mouse CD103	Biolegend	Cat# 121416
Ant-mouse MHC-II	Biolegend	Cat# 107632
Ant-mouse CD86	Biolegend	Cat# 105043
Ant-mouse PDL1	Biolegend	Cat# 124319
Ant-mouse Itgb7	Biolegend	Cat# 121007
Ant-mouse Ly6C	Biolegend	Cat# 128026
Ant-human Fab(2)'	Jackson ImmunoResearch	Cat# 109-066-006
Streptavidin-PE	Biolegend	Cat# 405204
Ant-human CD45	Invitrogen	Cat# 45-9459-42
Ant-human CD3	Biolegend	Cat# 317322
Ant-human CCR7	BD	Cat# 557648
Ant-human CD45RO	BD	Cat# 563722
Ant-human Tim3	Biolegend	Cat# 345032
Ant-human CD19	Biolegend	Cat# 302212
Ant-mouse CD209a	Biolegend	Cat# 833004
Ant-mouse IFN-gamma	Biolegend	Cat# 45-7311-82
Ant-mouse MHC-I/SIINFEKL	Biolegend	Cat# 141614
Ant-human CD86	Biolegend	Cat# 305420
Ova Tetramer	Biolegend	NIH Tetramer Core
TRP2 Tetramer	Biolegend	Cat# T03015
Anti-mouse CTLA4 (*in vivo*)	BioXcell	Cat# BE0131
Anti-mouse IFNaR (*in vivo*)	BioXcell	Cat# BE0241
Anti-mouse PD1 (*in vivo*)	BioXcell	Cat# BE0146
Bacterial and virus strains		
Stbl3 Competent Cells	UPenn Cell Center	N/A

REAGENT or RESOURCE	SOURCE	DENTIFIER
Biological samples		
Healthy human T cell donors	UPenn Human Immunology Core	N/A
Chemicals, peptides, and recombinant proteins		
Live/Dead Aqua	ThermoFisher	Cat# L34957
Syto RNASelect	ThermoFisher	Cat# S32703
Neutral Sphingomyelinase Inhibitor GW4869	SelleckChem	Cat# S7609
S1PR antagonist FTY720	SelleckChem	Cat# S5950
Poly I:C	Invivogen	Cat# Vac-pic
Critical commercial assays		
10X 3' Single Cell Sequencing Kit v2.0 v3.1	10X Genomics	Manufacturer Quote
NextSeq 500/550 v2.5	Illumina	Cat# 20024906
DynaBeads CD3x28 (Human)	ThermoFisher	Cat# 11131D
DynaBeads CD3x28 (Mouse)	ThermoFisher	Cat# 11453D
Deposited data		
M5BBz-7SL Human CAR-T	This paper	GEO: accession number GSE179249
CD45.2 Endogenous Immune Cells (CAR-T Treated)	This paper	GEO: accession number GSE179253
Experimental models: Cell lines		
B16-F10 Melanoma	ATCC	CRL-6475
B16-hCD19	This paper	N/A
TC1-huMesothelin	This paper	N/A
KP-hCD19	This paper	N/A
ASPC-1	This paper	N/A
Experimental models: Organisms/strains		
WT C57BL/6 (Charles River)	Charles River	Stock 027
WT CD45.1 C57BL/6 (Jackson)	Charles River	Stock 494
WT C57BL/6 (Jackson)	Jackson Labs	Cat# 000664
WT CD45.1 C57BL/6 (Jackson)	Jackson Labs	Cat# 002014
BATF3 KO Mice	Jackson Labs	Cat# 013755
TRAC KO Mice	Jackson Labs	Cat# 002116
RIG-I KO Mice	Jackson Labs	Cat# 46070-JAX
MAVS KO Mice	Jackson Labs	Cat# 008634
Oligonucleotides		
Human RN7SL1	This paper	N/A
Forward: GCT ACT CGG GAG GCT GAG GCT		
Reverse: TAT TCA CAG GCG CGA TCC		
Scramble RNA	This paper	N/A

REAGENT or RESOURCE	SOURCE	DENTIFIER
Forward: CTT CGC GGG AAC ATT CTC		
Reverse: GAC CGA GCT GGC ATC ATA TC		
Mouse IFNa7	This paper	N/A
Forward: CAT CTG CTG CTT GGG ATG GAT		
Reverse: TTC CTG GGT CAG AGG AGG TTC		
Mouse IFNa12	This paper	N/A
Forward: CAG CAG GTG GGG GTG CAG GAG		
Reverse: TTT CTT CTC TCT CAG GTA CAC		
Mouse IFNB	This paper	N/A
Forward: CTT TCG AAG CCT TTG CTC TG		
Reverse: CAG GAG AGC AAT TTG GAG GA		
Mouse GAPDH	This paper	N/A
Forward: AGG TCG GTG TGA ACG GAT TTG		
Reverse: TGT AGA CCA TGT AGT TGA GGT CA		
Mouse 18S	This paper	N/A
Forward: CCC CAT GAA CGA GGG AAT T		
Reverse: GGG ACT TAA TCA ACG CAA GCT T		
Human GAPDH	This paper	N/A
Forward: TGC ACC ACC AAC TGC TTA GC		
Reverse: GGC ATG GAC TGT GGT CAT GAG		
Human 18S	This paper	N/A
Forward: CCC CAT GAA CGA GGG AAT T		
Reverse: GGG ACT TAA TCA ACG CAA GCT T		
Recombinant DNA (plasmids)		
pMSGV h19BBz	This paper	N/A
pMSGV h19BBz-7SL	This paper	N/A
pMSGV h19BBz-Scr	This paper	N/A
pMSGV M5BBz	This paper	N/A
pMSGV M5BBz-7SL	This paper	N/A
pMSGV Ova-h19BBz	This paper	N/A
pMSGV Ova-h19BBz-7SL	This paper	N/A
pTRPE h19BBz-7SL	This paper	N/A
pTRPE M5BBz	This paper	N/A
pTRPE M5BBz-7SL	This paper	N/A
pTRPE M5BBz-Scr	This paper	N/A
pTRPE Ova-h19BBz	This paper	N/A
pTRPE Ova-h19BBz-7SL	This paper	N/A
pCLPs hCD19 (trunc)	This paper	N/A
Software and algorithms		
R Language and Environment	CRAN	https://cran.r-project.org/

REAGENT or RESOURCE	SOURCE	DENTIFIER
CellRanger	10X Genomics	https://www.10xgenomics.com/
SAVER (v1.1.2)	Huang et al., 2018	https://cran.r-project.org/web/packages/SAVER/index.html
Seurat (v3.1.2)	Stuart et al., 2019	https://satijalab.org/seurat/
Monocle (v2.12.0)	Qiu et al., 2017	https://www.bioconductor.org/packages/release/bioc/html/monocle.html
limma (v3.40.6)	Ritchie et al., 2015	https://bioconductor.org/packages/release/bioc/html/limma.html
GSVA (v1.32.0)	Hanzelmann et al., 2013	https://bioconductor.org/packages/release/bioc/html/GSVA.html